

ETH zürich

Frequency Modulation Cooling of an Ion in a Penning Trap

Noah Lehmann

D-PHYS

Trapped Ion Quantum Information Group

Supervisors:

Prof. Dr. Jonathan Home

Dr. Pavel Hrmo

Submitted to:

D-ITET

*In partial fulfillment of the requirements for the degree of Master of Science in
Quantum Engineering*

April 24, 2023

Abstract

Penning traps are used for quantum information processing on trapped ion qubits and for studying the fundamental properties of ions. For the successful execution of the experiments it is essential that the ions are cold. However, the magnetron motional mode of an ion in a Penning trap has negative energy, while the energies of the cyclotron and the axial mode are positive. Therefore, the ion can only be cooled if the standard Doppler cooling technique is modified. While there exist other schemes to do so, this thesis will focus on a novel approach which relies on modulating the cooling laser's frequency. The idea is to resonantly couple the magnetron mode to one of the modes with positive energy, which leads to an exchange of energy. By additionally detuning the cooling laser to the red of the cooling transition, overall kinetic energy is removed from all motional modes. The analysis will include an analytical treatment of the underlying physics, leading to a condition on the system parameters for cooling. Furthermore, including the stochastic nature of the ion-laser interaction and treating the resulting Langevin equation, an expression for the cooling rate and the cooling limit is derived. For the latter, numerical values of around $\bar{n}_- \approx 250$ and $\bar{n}_+ \approx 15$ are found for the magnetron and the cyclotron mode, respectively. Testing the scheme experimentally in the TIQI Penning trap, we find $\bar{n}_- = 280 \pm 30$ and $\bar{n}_+ = 3.1 \pm 0.3$.

Contents

Acknowledgements	v
1 Introduction	1
1.1 Penning Traps	2
1.1.1 Why Use a Penning Trap?	2
1.1.2 Dynamics in a Penning Trap	2
1.2 Laser Cooling Schemes	4
1.2.1 Doppler Cooling with Axialisation	5
1.2.2 Doppler Cooling with an Offset Beam	5
1.2.3 Frequency-Modulated Doppler Cooling	5
2 Parametric Oscillator and Cooling Condition	7
2.1 The Numerical Simulation	7
2.2 Radiation Pressure Force	9
2.3 Equations of Motion	9
2.3.1 Simplifying	9
2.3.2 Solving eq. (2.7)	10
2.4 Quality of the model	11
2.4.1 Taylor Approximation in the Stochastic Simulation	13
2.4.2 Further Procedure	14
3 Synchronisation and Cooling Mechanism	15
3.1 What is coupled?	15
3.2 Equations for Amplitude and Phase	15
3.2.1 In the rotating frame, following up on chapter 2	16
3.2.2 Starting from Zero	17
3.2.3 Cooling Condition Revisited	18
3.3 Visualisation of the Phase and Amplitude Trajectory	18
3.4 Spectrum Analysis of the Radiation Pressure Force	18
3.5 Higher Order Taylor Approximation	19
4 The Cooling Rate	22
4.1 Mathematics	22
4.1.1 The Change in Radii Squared: Δr_{\pm}^2	22
4.1.2 The Scattering Rate: γ_s	23
4.1.3 Multiplying and Averaging over the Ensemble	23
4.1.4 The coupling term	24
4.2 Visualisation of Synchronisation under a Stochastic force	25
4.2.1 The relation between θ_+ and θ_-	25

4.2.2	The Relation Between θ_c and n_-	27
4.2.3	Heating	28
4.3	Possibility for Different Cooling Schemes	29
4.3.1	Making Use of the Phase Control	29
4.3.2	Large Modulation Amplitude	31
5	Stochastic Differential Equation and Cooling Limit	32
5.1	Approach	32
5.2	Analytical Expression for the Cooling Limit	32
5.2.1	To Frequency Space and Back	33
5.2.2	Approximating as in eq. (2.6)	34
5.2.3	No Modulation	35
5.3	Cooling Limit for Numerically Obtained Bandstrengths	35
6	Experimental Implementation and Results	37
6.1	General Properties of the Setup	37
6.1.1	Penning Trap	37
6.1.2	Cooling Scheme	37
6.2	Converting Experimental Data to Phonon Numbers	37
6.3	Results	39
6.3.1	Comparison to Precool	39
6.3.2	Dependence on δ_0 and A_m	40
6.3.3	Resonance	40
6.3.4	Experimental Limits	40
7	Discussion	44
7.1	Theory	44
7.2	Experiment	44
7.3	Outlook	45
7.3.1	Possible Applications	45

List of Figures

1.1	The motion of an ion in a Penning trap in the radial plane at $z = 0$.	3
2.1	Illustration of the observed cooling.	8
2.2	Logarithm of the number of magnetron phonons as a function of δ_0 and A_m , from 2D simulation with orthogonal beams. Parameters are: $\omega_x = 2\pi \times 2$ MHz, saturation parameter $s_0 = 0.1$, $\omega_m = 2\omega_1$. Starting conditions are 2000 magnetron phonons, 100 cyclotron phonons.	12
2.3	Logarithm of the number of magnetron and cyclotron phonons as a function of δ_0 and A_m , gained from 3D stochastic simulation. Parameters are: $\omega_x = 2\pi \times 2$ MHz, saturation parameter $s_0 = 0.1$, $\omega_m = 2\omega_1$. Starting conditions are 2000 magnetron phonons, 100 cyclotron phonons. Datapoints are averages over 5ms in 'steady state'.	13
2.4	The same situation as in figure 2.3, but now with a scattering rate which is Taylor-approximated in the velocity. $\omega_x = 2\pi \times 2$ MHz, saturation parameter $s_0 = 0.1$, $\omega_m = 2\omega_1$. Starting conditions are 2000 magnetron phonons, 100 cyclotron phonons.	14
3.1	Illustration of the coupling mechanism in frequency space. Green is the ion's motion, orange is the radiation pressure force. Through F_{RP} the cyclotron and the magnetron are coupled.	16
3.2	Simulation of phonons and phase as function of time, based on eq. (2.5), for coefficients $\omega_m = \omega_c$, $A_m = 2\pi \times 18$ MHz, $\delta_0 = 2\pi \times 10$ MHz, $s = 0.5$. Depending on θ_c , either the cyclotron or the magnetron mode is cooled.	19
3.3	Bandstrengths as a function of detuning and modulation amplitude for 2 MHz trapfrequency and 0.1 intensity saturation. For large A_m we observe that $c_0 < 0$ and comparing the two we can find the region in which the cooling condition (3.13) is fulfilled.	20
3.4	The logarithm of $-c_{30}$ as a function of detuning and modulation amplitude. Where $c_{30} > 0$, the bandstrength was set to -100.	21
4.1	Relation of θ_+ at $\omega_m = \omega_c$, $A_m = 2\pi \times 22$ MHz, $\delta_0 = 2\pi \times 10$ MHz, $s_0 = 0.5$, where datapoints are selected according to whether the modes are heating or cooling. The colours indicate the number of incidents counted.	26
4.2	Visualisation of the correlation between θ_c and the time derivative in magnetron phonons. $A_m = 2\pi \times 20$ MHz, $\delta_0 = 2\pi \times 6$ MHz, $s_0 = 0.1$.	27
4.3	Correlation check for θ_c and the number of phonons at $\omega_m = \omega_c$, $A_m = 2\pi \times 22$ MHz, $\delta_0 = 2\pi \times 15$ MHz and $\delta_0 = 2\pi \times 0$ MHz, $s_0 = 0.5$. The phase is 'locked' to π and 0, respectively, depending on whether the detuning is 'too big' or 'too small'.	28
4.4	θ_c over time for varying initial phase at $\omega_m = \omega_c$, $A_m = 2\pi \times 22$ MHz, $\delta_0 = 2\pi \times 15$ MHz and $s_0 = 0.5$. The fluctuations die off once both modes are hot.	29
4.5	Phase-controlling at $\omega_m = 2\omega_1$, $A_m = 2\pi \times 22$ MHz, $s_0 = 1.5$, alternating between $\delta_0 = 0$ MHz and $\delta_0 = 2\pi \times 4$ MHz. As long as neither of the modes goes too cold, we can control θ_1 .	30

4.6	Phonons over time for varying initial phase at $\omega_m = \omega_- + \omega_z$, $A_m = 2\pi \times 62$ MHz, $\delta_0 = 2\pi \times 6$ MHz and $s_0 = 0.5$ with an additional axial unmodulated $\delta_z = 2\pi \times 6$ MHz, $s_0 = 0.013$ beam. Phonons are exchanged between the magnetron and the axial mode.	31
5.1	Cooling limit in the cyclotron mode as a function of δ_0 and A_m .	36
5.2	Cooling limit in the magnetron mode as a function of δ_0 and A_m .	36
5.3	Numerical cooling limits as function of detuning and modulation amplitude, at $f_x = 2$ MHz trap frequency and $s = 0.1$ 0.1 saturation intensity. In the region where the cooling condition (3.13) is not fulfilled, the limit was set to 100 and 1000, respectively. The limit lies around 10 phonons for the cyclotron and around 250 for the magnetron mode.	36
6.1	The beam configuration that was utilized and the trap surface. The cooling beam is denoted Detection, while the Raman beams control the qubit state. Figure by Shreyans Jain.	38
6.2	Experimental setup for generating the cooling and the repump beam. NDD denotes 'near-detuned-detection' and FDD represents the 'far-detuned-detection'. The light entering the cavities has a wavelength of 626 nm, which is halved to 313 nm. Figure by Shreyans Jain.	38
6.3	Excitation of the magnetron motional sidebands 0, +3, +6, +9, +12 (from left to right) as a function of the pulse duration of the modulated cooling following the precooling.	40
6.4	Experimental cooling as function of detuning and modulation amplitude. The ratio between the excitation probabilities of the sideband and the carrier is an indication of the coolest point, with a higher ratio corresponding to lower \bar{n}_- .	41
6.5	Excitation of the magnetron motional sidebands 0, +2, +4, +6, +8 (from left to right) as a function of the modulation frequency.	42
6.6	Excitation lineshapes of the magnetron motional sidebands 0, +3, +6, +9, +12 (from left to right). The number of included magnetron mode Fockstates is 1000. $\bar{n}_- = 280 \pm 30$ and $\bar{n}_+ = 3.1 \pm 0.3$.	42
6.7	Excitation lineshapes of the axial red sidebands 0-4 (from left to right). The number of included axial Fockstates is 150. $\bar{n}_z = 6.8 \pm 0.4$.	42

Acknowledgements

I would like to express my heartfelt gratitude to the Penning team, Dr. Pavel Hrmo, Shreyans Jain and Tobias Sägeser, for their exceptional support, guidance, and expertise throughout my research journey. Their valuable contributions, insightful feedback, and unwavering dedication have been indispensable to the successful completion of this thesis.

I would also like to thank my thesis advisor, Prof. Dr. Jonathan Home, for his support and guidance during this project. His expertise and knowledge were valuable resources, and I am grateful for his contributions.

Finally, I would like to express my sincere gratitude to my friends and family for their support, encouragement, and motivation throughout my academic journey. Special thanks go to Claire Schrago, my proofreader, for her dedicated feedback and assistance in refining the linguistic quality of this work. Her expertise and attention to detail have been invaluable to the success of my thesis.

Thank you all for your precious contributions to my academic and personal growth.

Chapter 1

Introduction

Quantum computers promise an exponential speedup in the processing of certain problems compared to classical computers [1]. This is done by running quantum algorithms which are designed to take advantage of the quantum bits (qubits) on which the quantum computer is based, for example, to factorize integers into prime numbers Shor's algorithm can be employed [2]. Furthermore, quantum computers in the shape of quantum simulators can be used to efficiently simulate physical systems on a quantum level [3]. Therefore, extensive research is being conducted to develop a suitable platform for quantum computing, and one promising approach is the use of trapped ions, a field of study in the TIQI group at ETHZ.

When trapped ions are used as qubits, the two-level system is usually implemented in the ions' internal electronic levels. Multi-qubit gates are performed by coupling the ions via a shared motional mode, for example in the Cirac-Zoller gate [4]. Trapped-ion qubits have the advantage that each ion is identical to the other (if the same species is chosen), while scaling up the system is difficult.

In order for successful quantum information processing to be feasible on trapped ion qubits, one of many requirements is that the ions are 'cold', meaning that their vibrational motion in the trap is small and slow. While certain operations, as for example the aforementioned Cirac-Zoller gate, require cold ions in the ground state of motion for successful implementation, there are much more fundamental reasons to why we require the ions to be cold. One of them is that we want to operate in the Lamb-Dicke regime, where the change in kinetic energy due to the absorption of a photon is small compared to one motional quantum of energy. This means that the coupling between the internal and the motional state is minor, as the chance that the ion's motion is excited due to the absorption of a photon then is small. Another, more spectroscopic, reason is that we want to control the ion's internal states using lasers. In order to make these operations as precise as possible, it is essential that the laser's frequency is set correctly. However, even if we set it perfectly, the precision of the experiment can suffer greatly if the ion is hot, i.e. oscillating at great velocity inside the trap. Then, the ion's absorption frequency is broadened owing to the Doppler effect, which is known as Doppler broadening.

As a consequence, it is essential to be able to cool trapped ions. For many applications, the ions are wanted in the motional ground state which is achieved by driving their motional sidebands, a technique called 'resolved sideband cooling'. Thereby, quanta of motional energy are traded for quanta of internal energy, which is more rigorously discussed in [5]. For this to be efficiently feasible, we require the ions to be relatively cold to begin with.

The standard technique to arrive at this intermediate step this is Doppler-cooling. Here, a laser is directed at an ion (or atom) which has a cycling transition. This means that the electronic state cycles repeatedly between two levels, as it is excited after absorbing a photon, which it then quickly re-emits, decaying to the initial internal state. The laser then is detuned to the red of this transition and therefore, the ion absorbs photons primarily as it moves towards the source, because then the Doppler effect compensates for the red detuning by shifting the frequency to the blue. Since the photons are re-emitted in random directions, the net effect of the scattering on the ion is a friction opposing the laser's direction. Hence, an ion harmonically oscillating to and fro loses energy until there

is an equilibrium between the random photon scattering and the friction. A more thorough treatment of this is provided in [6].

Thus, for laser-cooling, it would be ideal to trap an ion in a three-dimensional quadratic electric potential, inducing harmonic oscillations in three directions. However, according to Earnshaw's theorem this is not feasible: It states that the Laplace equation $\Delta\phi = 0$ holds for ϕ being the electrical potential. There exist different approaches to deal with this issue, one of the notable ones being the Penning trap, which we will explore more closely in this chapter. In this trap, an axial quadratic potential is used in combination with a magnetic field, such that the Lorentz force keeps the ion radially trapped. However, in this geometry there arise two motional modes in the radial plane, one of which has negative energy, i.e. it is not stable and removing its energy through the means of red-detuned Doppler cooling will increase its motional amplitude. There are various techniques available to manage this issue, but each method is accompanied by its own set of limitations. Thus, a novel way of cooling all the motional modes of an ion in a Penning trap is explored in this thesis, which relies on frequency-modulating the cooling laser.

1.1 Penning Traps

An ideal Penning trap consists of two building blocks, one of which is a quadratic electrical potential which is confining in the axial (\hat{z}) direction and anti-confining in the radial (\hat{x}, \hat{y}) plane:

$$\phi(x, y, z) = \phi_0 \left(z^2 - \frac{x^2 + y^2}{2} \right). \quad (1.1)$$

To trap the ion in the radial plane, a strong, homogeneous magnetic field is applied along the axial direction, $\mathbf{B} = B_0\hat{z}$, which is the other block. Therefore, the Lorentz force keeps the ion in the trap as it is pushed out by the anti-confining potential.

1.1.1 Why Use a Penning Trap?

Penning traps are a great tool to study the physical properties of particles, as e.g. described in [7], and can be used for performing quantum information and simulation experiments on trapped ions [8].

Comparing the Penning trap to the more widely-used Paul trap, we find that while cooling Penning ions is more challenging than it is with Paul ions, the Penning trap offers other advantages. Possibly the most prominent one is the low heating rates one can achieve [9], which may be because no rotating quadrupole potential has to be applied to keep the ion in the trap. Meanwhile this potential is a source of excess micromotion in Paul traps, as further explored in [10]. Furthermore, the fact that no rotating quadrupole potential is needed may simplify the engineering significantly when moving to larger numbers of trapped ions.

1.1.2 Dynamics in a Penning Trap

Motional Modes

From the previously provided description of the ideal Penning trap, we can now straightforwardly find the dynamics of a classical trapped ion with mass m and electrical charge e . In the axial direction, the equation of motion simply reads

$$m\ddot{z} = -2e\phi_0 z, \quad (1.2)$$

so the axial motion is that of a harmonic oscillator with frequency $\omega_z = \sqrt{\frac{2e\phi_0}{m}}$.

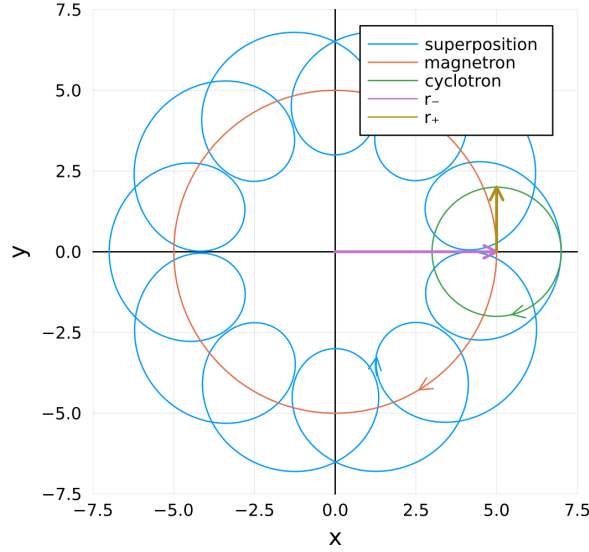


Figure 1.1: The motion of an ion in a Penning trap in the radial plane at $z = 0$.

Meanwhile, in the radial plane, we have two acting forces, namely the electrostatic force from the electric field and the Lorentz force from the magnetic one. It follows that

$$\ddot{x} = \frac{\omega_z^2}{2}x + \omega_c \dot{y} \quad (1.3a)$$

$$\ddot{y} = \frac{\omega_z^2}{2}y - \omega_c \dot{x}, \quad (1.3b)$$

where we define the unmodified cyclotron frequency as $\omega_c = \frac{eB_0}{m}$. To find the eigenmodes of the radial motion, it is convenient to associate the radial plane with the complex plane $\mathbb{R}^2 \cong \mathbb{C}$. Then, every point on the radial plane corresponds to a complex number:

$$\begin{bmatrix} x \\ y \end{bmatrix} \cong u = x + iy. \quad (1.4)$$

The ion's radial motion then is described by the real and imaginary part of

$$\ddot{u} + i\omega_c \dot{u} - \frac{\omega_z^2}{2}u = 0, \quad (1.5)$$

for which we can make the Ansatz $u = Ae^{i\omega t}$, as we expect the solution to be a rotating motion around the origin. Inserting said Ansatz, we get a quadratic equation in ω , with the solutions

$$\omega_{\pm} = \frac{\omega_c \pm \sqrt{\omega_c^2 - 2\omega_z^2}}{2} \equiv \frac{\omega_c}{2} \pm \omega_1. \quad (1.6)$$

Consequently, the ion's radial motion is a superposition of the two modes of motion in the radial plane, which are the (modified) cyclotron at the higher frequency ω_+ and the magnetron mode oscillating at the lower ω_- . This is depicted in figure [1.1](#). The condition that we must have real frequencies imposes the following boundary on the axial frequency:

$$\omega_z^2 \leq \frac{\omega_c^2}{2}. \quad (1.7)$$

For the ion to be considered "cool", i.e. in order to prevent the Doppler broadening from deteriorating our precision and for the motion to be sufficiently decoupled from the internal states, each of the three modes of

motion needs to be cool.

Energy and Complications with Doppler Cooling

While we can already confidently assume that the harmonic axial motion can be cooled with standard red-detuned Doppler-cooling, as described earlier, the same should not be done for the radial modes of motion.

With the purpose of illustrating this, we shall find an expression for the total energy $E_t = E_{kin} + E_{pot}$ of the system, starting from the cartesian expression of the coordinates:

$$z(t) = r_z \cos(\omega_z t + \theta_z) \quad (1.8a)$$

$$x(t) = r_- \cos(\omega_- t + \theta_-) + r_+ \cos(\omega_+ t + \theta_+) \quad (1.8b)$$

$$y(t) = -r_- \sin(\omega_- t + \theta_-) - r_+ \sin(\omega_+ t + \theta_+), \quad (1.8c)$$

where r_{\pm} denotes the amplitude or the radius of the cyclotron and the magnetron motion, respectively. Inserting this into $E_{kin} = \frac{mv^2}{2}$ and $E_{pot} = e\phi$, we find the total energy

$$E_t = \frac{m}{2} (r_z \omega_z^2 + 2r_+^2 \omega_+ \omega_1 - 2r_-^2 \omega_- \omega_1). \quad (1.9)$$

We notice that, while the energy increases with increasing axial and cyclotron amplitude, as one would expect, it actually decreases with increasing magnetron amplitude, wherefore the magnetron mode is unstable. Consequently, to reduce the magnetron amplitude, i.e. cool the magnetron (reduce its kinetic energy), energy needs to be added to the mode, while removing energy from it heats it.

Thus, if we wanted to Doppler-cool the magnetron, we would need the frequency to be blue-detuned from the ion's transition, which in return would heat up the cyclotron. This effect is, for example, explored in [11] but will also be addressed in this thesis. As the ion is continuously heated up due to noise and trap imperfections, if we do not find a way to cool both radial modes simultaneously, the ion will inevitably be heated out of the trap.

Phonons and Energy

The classical motion of the ion can be quantised as described in [12] and as a consequence the energy contained in a motional mode is measured in quanta of motion, namely phonons. The phonon number in the radial modes is given by

$$n_{\pm} = \frac{r_{\pm}^2 m \omega_1}{\hbar}, \quad (1.10)$$

where the radii or amplitudes of the modes can be extracted from eq.s (1.8), yielding

$$r_{\pm}^2 = \frac{1}{4\omega_1^2} ((\omega_{\mp} x + \dot{y})^2 + (\omega_{\mp} y - \dot{x})^2). \quad (1.11)$$

Similarly, the axial number of phonons relates to the amplitude of its motion according to

$$n_z = \frac{r_z^2 m \omega_x}{2\hbar}. \quad (1.12)$$

1.2 Laser Cooling Schemes

As already indicated, different schemes have been developed which have the goal of overcoming the problems created by the magnetron's negative energy, two of which we shall allude to here. A third one will be the topic of this thesis. Primarily, the point of these schemes is getting the ion cold enough for it to be sideband-cooled to its motional ground state.

1.2.1 Doppler Cooling with Axialisation

One way of cooling both radial modes is to apply a weak electric quadrupole potential rotating at the true cyclotron frequency ω_c :

$$\phi_{ax}(t) = \phi_{ax,0} (x^2 - y^2) \cos(\omega_c t). \quad (1.13)$$

This is, for example, described thoroughly in [13]. This potential couples the magnetron to the cyclotron mode, leading to an exchange of energy. Overall, the energy is then removed from the system by adding a single standard, red-detuned Doppler-cooling beam to the setup, cooling the cyclotron (and the axial) mode.

While this method achieves very low cooling limits [14], we add a source of micromotion by adding the rotating potential. Thus, the main advantage that a Penning trap has over a Paul trap has to be given up, though we should keep in mind that the rotating potential does not have to be as strong, i.e. the induced excess micromotion is smaller than it is in a Paul trap. Nevertheless, the locations where ions can be trapped without picking up excess micromotion from the rotating potential are limited to the RF null.

1.2.2 Doppler Cooling with an Offset Beam

A different idea is to use the non-uniformity of the (red-detuned) cooling laser beam to achieve simultaneous cooling in both radial modes. The beam is offset from the center of the motion such that its intensity is highest where the slow magnetron motion is leading the ion away from the laser source. However, including the fast cyclotron motion in this consideration, the net motion still sometimes points towards the beam such that the Doppler effect leads to resonance. If then a photon is absorbed, the magnetron gains, while the cyclotron mode loses energy, and due to the magnetron mode's negative energy, both modes' radii shrink and are cooled. Of course, on the other side of the trajectory, there will be events where the cyclotron is cooled, and the magnetron is heated, but due to the intensity gradient, their rate of occurrence will be lower. This is more extensively discussed in [11].

1.2.3 Frequency-Modulated Doppler Cooling

Another possibility of cooling all the motional modes of a Penning ion at once is based on modulating the frequency of a cooling laser which is red-detuned from the cycling transition. In other words, the detuning is then time-dependent

$$\delta(t) = \delta_0 + A_m \cos(\omega_m t), \quad (1.14)$$

where ω_m is the modulation frequency, δ_0 is the detuning and A_m is the modulation amplitude. We will find and discuss that if the modulation frequency is the difference or the sum of the two radial frequencies

$$\omega_m = \omega_+ + \omega_- = \omega_c, \quad (1.15a)$$

$$\omega_m = \omega_+ - \omega_- = 2\omega_1, \quad (1.15b)$$

the two motional modes are resonantly coupled, thereby leading to energy exchange, similar to what we observe when applying axialisation. The overall energy is then removed from the system due to the red detuning, $\delta_0 > 0$.

Generally, we will focus our analysis on the radial plane, mostly ignoring the axial mode. However, when the cooling beam has a projection on both the radial plane and the \hat{z} -axis, the cooling scheme also works when modulating at $\omega_m = \omega_x \pm \omega_-$, coupling the magnetron to the axial mode.

This cooling scheme will be the topic of this thesis. In chapter 2, we will find the first condition on the parameters for observing cooling. To do so, we will move to a rotating frame and treat the radiation pressure force as a parametric drive while neglecting the fluctuations in the force, occurring due to the individual photon scattering events. Furthermore, the methods used in the numerical simulations will be briefly addressed. Chapter 3 will focus on the cooling mechanism, where we treat the ion's dynamics as a synchronisation problem. We will examine the resonance and retrieve a second version of the cooling condition, all while still treating the ion-laser interaction in the same averaged sense as in the previous chapter. Then, to find the cooling rate and its limit, we will also include

the fluctuation of the force which leads us to a Langevin-type equation. As a consequence, in chapter 4 we will discover equations describing the rate of change in the radial modes' radii by finding the change in radius squared per photon scattering event, multiplying this by the scattering rate and taking the ensemble average. To conclude the theoretical treatment, in chapter 5 we will identify the cooling limit for the magnetron and the cyclotron mode by moving to frequency space and making use of the fact that the fluctuations in the radiation pressure force are white noise. In this process, our analytically theoretical results will be compared to numerical simulations of the system. The theoretical treatment is compared to experimental data in chapter 6. The data is obtained from the TIQI Penning trap, which was adapted to the requirements of the frequency modulation scheme. Finally, chapter 7 will conclude the thesis and provide an outlook.

Chapter 2

Parametric Oscillator and Cooling Condition

We are looking for an analytical theory behind frequency modulation cooling. Modulating the laser frequency leads to a detuning as described by eq. (1.14), where the modulation frequency has to be set as described in eq.s (1.15) in order for resonance effects and, therefore, cooling to occur.

In this chapter, we will first examine the numerical software used to simulate frequency modulation cooling. Then, in the analytical part of this chapter, we shall, for simplicity, treat the laser's force as its average, neglecting the fluctuations created by the randomness of the photon scattering. Thus, we will investigate the system's dynamics by moving to a rotating frame in which the force exerted by the laser on the ion is modulated at twice the motional frequencies. This then corresponds to parametric oscillation and can be treated accordingly. Finally, by determining the system's eigenvalues we will see what parameters of the system decide if cooling occurs or not and find the dynamics of the motional amplitudes r_{\pm} depending on the detuning and the modulation amplitude.

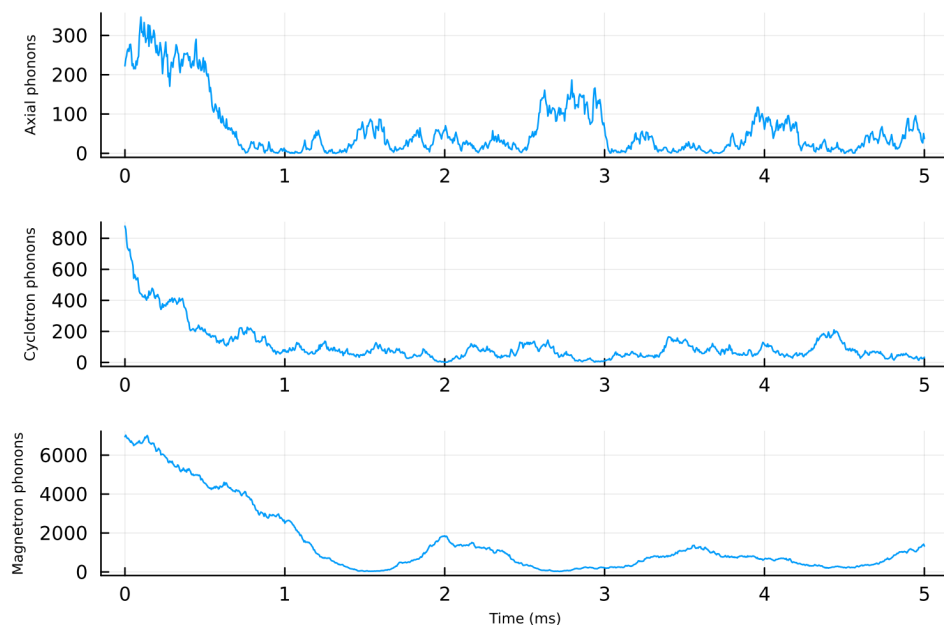
2.1 The Numerical Simulation

Before we indulge in this theoretical treatment, we ought to have a quick look at the numerical simulations, in which the frequency modulation cooling was first observed and which will be referenced repeatedly throughout this thesis.

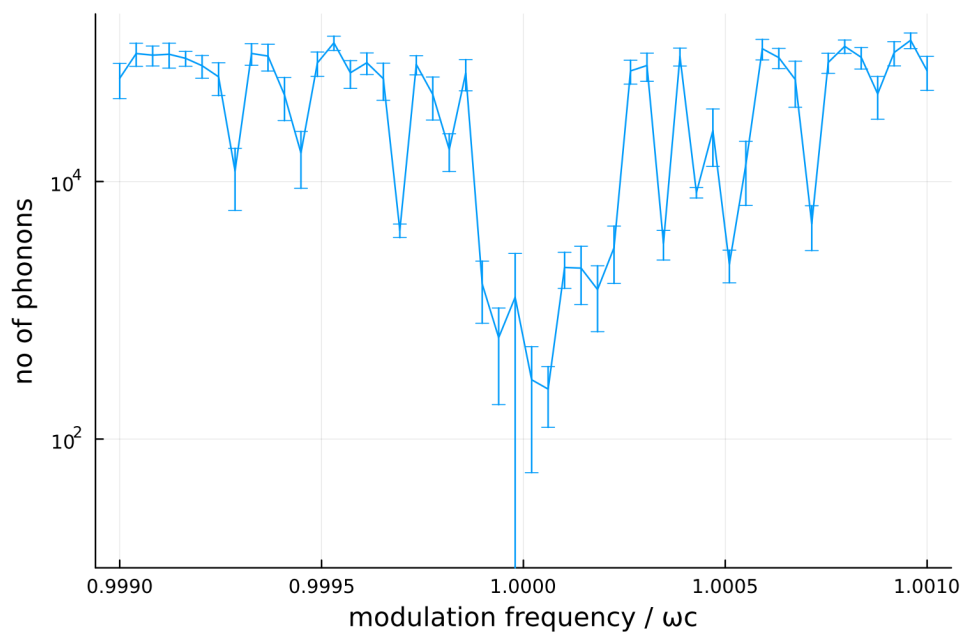
Two main simulations are used, one of which describes the stochastic process of the laser-ion interaction, while the other treats this interaction (i.e. the radiation pressure force) as its average and is, therefore, numerically simple. Both simulations are implemented in a Julia notebook, where the ion's dynamics are defined as described in section 1.1.2.

The interaction between the ion and the laser in the stochastic simulation is implemented as a 'JumpProcess' making use of the 'SortingDirect' method, which significantly improves the performance of the simulation of stochastic processes. On a physical level, each jump event corresponds to the absorption of a photon from the laser and the consecutive re-emission of said photon in a random direction. The scattering rate is given by the scattering cross section (which depends on the detuning and the ion's velocity) times the laser's intensity. The 'Tsit5' solver is used to solve the problem, where both the relative and absolute tolerance are set to 10^{-6} .

Some results of this stochastic simulation are displayed in figure 2.1. Figure 2.1a shows that all three modes can be resonantly cooled with the same laser beam if the parameters are set correctly. Meanwhile, in figure 2.1b we scan the cooled magnetron phonon number over the modulation frequency, where we find that the ion only gets cooled in a narrow range, approximately 1 kHz wide, around the resonance frequency $\omega_m = \omega_c$ (the same holds for $\omega_m = 2\omega_1$). The data points are an average over 4 ms, during which the ion is considered in a 'steady state', i.e. the cooling process should be over (in the case where heating is observed, this naturally is not the case). The



(a) Phonons over time in the three modes for $\omega_m = \omega_c$, $A_m = 2\pi \times 20$ MHz, $\delta_0 = 2\pi \times 6$ MHz.



(b) Frequency scan for magnetron phonons around the resonance frequency ω_c , starting at 3000 phonons. $A_m = 2\pi \times 20$ MHz, $\delta_0 = 2\pi \times 6$ MHz. The resonant frequency region is roughly 1 kHz wide.

Figure 2.1: Illustration of the observed cooling.

errorbars come from taking the standard deviation of the fluctuation in phonon numbers during this time.

2.2 Radiation Pressure Force

Turning back to analytical theory, we want to describe the ion in a Penning trap (as seen in section 1.1.2) and its averaged interaction with the laser. The mean force the laser exerts on the ion is the radiation pressure force:

$$F_{RP}(\mathbf{v}, t) = \frac{\hbar k \Gamma \Omega_1^2}{4} \frac{1}{(\delta(t) + \mathbf{k} \cdot \mathbf{v})^2 + \left(\frac{\Gamma}{2}\right)^2 + \frac{\Omega_1^2}{2}}, \quad (2.1)$$

where $\frac{\Omega_1^2}{2} = \frac{\Gamma^2}{4} s$ is the Rabi frequency, Γ is the decay rate, s is the saturation parameter and \mathbf{v} is the ion's velocity. For small velocities, this expression can be Taylor expanded as

$$F_{RP}(\mathbf{v}, t) \approx F_{RP}(0, t) - \zeta(t) \mathbf{v}, \quad (2.2)$$

where we define the friction parameter as

$$\zeta(t) = \frac{\hbar k^2 \Gamma \Omega_1^2}{2} \frac{\delta(t)}{\left(\delta(t)^2 + \left(\frac{\Gamma}{2}\right)^2 + \frac{\Omega_1^2}{2}\right)^2}. \quad (2.3)$$

2.3 Equations of Motion

Focusing on the radial plane and associating it with the complex one, defining $u = x + iy$ as in section 1.1.2, we can write down the differential equation describing the ion dynamics, which reads

$$\ddot{u} + i\omega_c \dot{u} + \zeta(t) \dot{u} - \frac{\omega_z^2}{2} u = F_{RP}(0, t). \quad (2.4)$$

Simulating this, we encounter cooling for $\omega_m = 2\omega_1$, however, $\omega_m = \omega_c$ only leads to cooling if we implement our damping in just one direction, e.g. have a damping term only in x-direction as in

$$\frac{d^2x}{dt^2} - \omega_c \frac{dy}{dt} + \zeta(t) \frac{dx}{dt} - \frac{\omega_z^2}{2} x = F_{RP}(0, t), \quad (2.5a)$$

$$\frac{d^2y}{dt^2} + \omega_c \frac{dx}{dt} - \frac{\omega_z^2}{2} y = 0. \quad (2.5b)$$

The reason is that in eq. (2.4) no resonant band coupling the motional modes can be found for $\omega_m = \omega_c$, which will become more clear during the discussion in chapter 3.

The formulation of eq.s (2.5) represents the setup where we have one beam only (here in x-direction), because only the motion in x-direction gets damped. If we want to have one beam, but stick to the complex equation like (2.4), we can replace \dot{u} by $\Re[\dot{u}] = \frac{1}{2}(\dot{u} + \bar{\dot{u}})$.

2.3.1 Simplifying

From the simulation, it becomes evident that the force term, which is responsible for the cooling, is the numerator in $\zeta(t)$ (defined in (2.3)), while $F_{RP}(0, t)$ (cf. (2.1)) solely leads to an oscillating offset. The time dependence in the denominator of $\zeta(t)$ affects the cooling, but to understand the mechanism it is not necessary and, therefore, its

inclusion is postponed to chapter 3. Hence, we neglect $F_{RP}(0, t)$ (i.e. do a variable shift) and for now approximate

$$\zeta(t) \approx \frac{\hbar k^2 \Gamma \Omega_1^2}{2} \frac{\delta(t)}{\left(\delta_0^2 + \frac{\Gamma^2}{2} + \frac{\Omega_1^2}{2}\right)^2} =: \zeta_0 \delta(t). \quad (2.6)$$

This approximation drastically simplifies the differential equation of interest, (2.4), to

$$\ddot{u} + \dot{u} \left(i\omega_c + \zeta_0 (\delta_0 + A_m \cos(\omega_m t)) \right) - u \frac{\omega_z^2}{2} = 0. \quad (2.7)$$

2.3.2 Solving eq. (2.7)

In this "2-beam description", we set $\omega_m = 2\omega_1$ to keep the resonant coupling terms. We notice that the system parameters change at twice the frequency of the motion if we move to a frame rotating at $\frac{\omega_c}{2}$. Therefore, to solve eq. (2.7), we treat the ion-laser system as a parametric oscillator. We start by doing a coordinate transformation of

$$q(t) := e^{D(t)} u(t), \quad (2.8)$$

where

$$D(t) = \frac{1}{2} \int i\omega_c + \zeta_0 (\delta_0 + A_m \cos(\omega_m \tau)) d\tau. \quad (2.9)$$

This moves us into a frame rotating at $\frac{\omega_c}{2}$ and q grows exponentially compared to u . Consequently, if we can make q grow with an exponential factor smaller than $e^{\frac{1}{2}\zeta_0\delta_0 t}$, we achieve the desired cooling.

The transformation in (2.8) now allows us to rewrite the differential equation (2.7) as

$$\frac{d^2 q}{dt^2} + \Omega(t)^2 q = 0, \quad (2.10)$$

where we define

$$\Omega^2(t) := -\frac{\omega_z^2(t)}{2} - \frac{1}{2} \frac{d\zeta_0 \delta(t)}{dt} - \frac{1}{4} (i\omega_c + \zeta_0 \delta(t))^2 := \omega_n^2 (1 + f(t)), \quad (2.11)$$

in which ω_n is the natural frequency of the oscillator and $f(t)$ is the pumping function. Neglecting terms quadratic in ζ_0 (which is reasonable as it's vanishingly small if we decrease the laser power), we get

$$\omega_n^2 \approx \omega_1^2 - \frac{i}{2} \omega_c \zeta_0 \delta_0, \quad (2.12a)$$

$$\omega_n^2 f(t) \approx -\frac{i}{2} A_m \zeta_0 (\omega_+ e^{i2\omega_1 t} + \omega_- e^{-i2\omega_1 t}). \quad (2.12b)$$

It follows that the parametric pumping function $f(t)$ oscillates at roughly $2\omega_n$. This is important because then the product $f(t)q$ will have a band oscillating at resonance.

Now we make the Ansatz

$$q(t) = C(t)e^{i\omega_1 t} + B(t)e^{-i\omega_1 t}, \quad (2.13)$$

where $B(t)$ and $C(t)$ are slowly varying amplitudes (associated with the cyclotron $\propto e^{-i\omega_+ t}$ and the magnetron motion $\propto e^{-i\omega_- t}$, respectively), such that their second derivative is negligibly small, $\ddot{B} \approx \ddot{C} \approx 0$. Considering this, we find that

$$\ddot{q} = 2i\omega_1 \dot{C} e^{i\omega_1 t} - \omega_1^2 C e^{i\omega_1 t} - 2i\omega_1 \dot{B} e^{-i\omega_1 t} - \omega_1^2 B e^{-i\omega_1 t}.$$

Inserting into eq. (2.10) and neglecting terms which are not oscillating near the natural frequency $\omega_n \approx \pm\omega_1$ (which is sensible as they do not contribute significantly to resonance), we get two coupled differential equations,

one each for terms oscillating at $e^{\pm i\omega_1 t}$:

$$\frac{d}{dt} \begin{bmatrix} C(t) \\ B(t) \end{bmatrix} = \frac{\zeta_0}{4\omega_1} \begin{bmatrix} \omega_c \delta_0 & A_m \omega_+ \\ -A_m \omega_- & -\omega_c \delta_0 \end{bmatrix} \times \begin{bmatrix} C(t) \\ B(t) \end{bmatrix}. \quad (2.14)$$

We now want to solve this for eigenvalues corresponding to a solution of the form

$$\begin{bmatrix} C(t) \\ B(t) \end{bmatrix} = c_+ \vec{V}_+ e^{\lambda_+ t} + c_- \vec{V}_- e^{\lambda_- t}. \quad (2.15)$$

The subscripts are not connected to the cyclotron or the magnetron motion, but purely to the eigenvalues of the matrix in eq. (2.14), which are given by

$$\lambda_{\pm} = \pm \frac{\zeta_0}{8\omega_1} \sqrt{-4(A_m^2 \omega_+ \omega_- - \omega_c^2 \delta_0^2)}. \quad (2.16)$$

Considering the transformation back to $u(t) = q(t)e^{-D(t)}$, with $D(t)$ as described in eq. (2.9), the back-transformed amplitudes C' , B' decay (i.e. we achieve cooling) if $\lambda_{\pm} t - D(t)$ is decreasing, i.e. if $\Re(\lambda_{\pm}) < \frac{1}{2}\zeta_0 \delta_0$, or written out:

$$\Re\left(\pm \sqrt{-4(A_m^2 \omega_+ \omega_- - \omega_c^2 \delta_0^2)}\right) < 4\delta_0 \omega_1. \quad (2.17)$$

In the case in which the expression in the square root in eq. (2.17) is positive, this is equivalent to the condition that

$$A_m > 2\delta_0, \quad (2.18)$$

given that $\omega_c > 2\omega_1$ (which always holds).

Meanwhile, a negative expression in the square root in eq. (2.17) leads to a modified oscillation frequency according to eq. (2.15). Then, if $\left|\sqrt{-4(A_m^2 \omega_+ \omega_- - \omega_c^2 \delta_0^2)}\right|$ becomes large, the amplitudes B and C start oscillating quickly, meaning that our neglecting \ddot{C} , \ddot{B} becomes inappropriate. This is the case if A_m becomes large and δ_0 remains small.

2.4 Quality of the model

Eq. (2.18) is the cooling condition in this simplified theoretical model. Of course, the model is not entirely accurate, and to assess its quality, we shall simulate its dynamics and compare the ‘steady state’ average phonon number as a function of δ_0 and A_m (respectively its logarithm) to that of other models, which can be assumed to be more accurate. We will stick to the magnetron phonon number because it turns out that generally, the magnetron mode is (relatively) cold if and only if the cyclotron mode is cold, so it suffices to look at one of them (see fig. 2.3). As described in section 2.1, the data points are taken by running the simulation until the system is assumed to be in a steady state, at which point the phonon number is averaged over an additional simulation period.

Figure 2.2a shows the aforementioned simulation for the model we have been working with, with simplified damping coefficient $\zeta(t)$ as in eq. (2.6). As expected, the plot displays the heating-cooling boundary around $A_m = 2\delta_0$. Everything below that line leads to great cooling (except for $\delta_0 = 0$). Furthermore, for increasing A_m , the boundary starts to dip. This is because there the cooling rate is lower and, therefore, the steady state has not been reached yet after the simulated 2.5 ms.

In figure 2.2b we see the results of a very similar simulation, but now using the real damping coefficient, $\zeta(t)$ as in eq. (2.3). We recognize the cooling boundary, which now is slightly shifted. However, below the boundary, heating occurs for medium and large δ_0 and A_m .

Figure 2.3 displays the logarithm of the phonon number in the magnetron and the cyclotron mode as a function of δ_0 and A_m in the 3D simulation, which considers the individual photon scattering events and a non-linearised

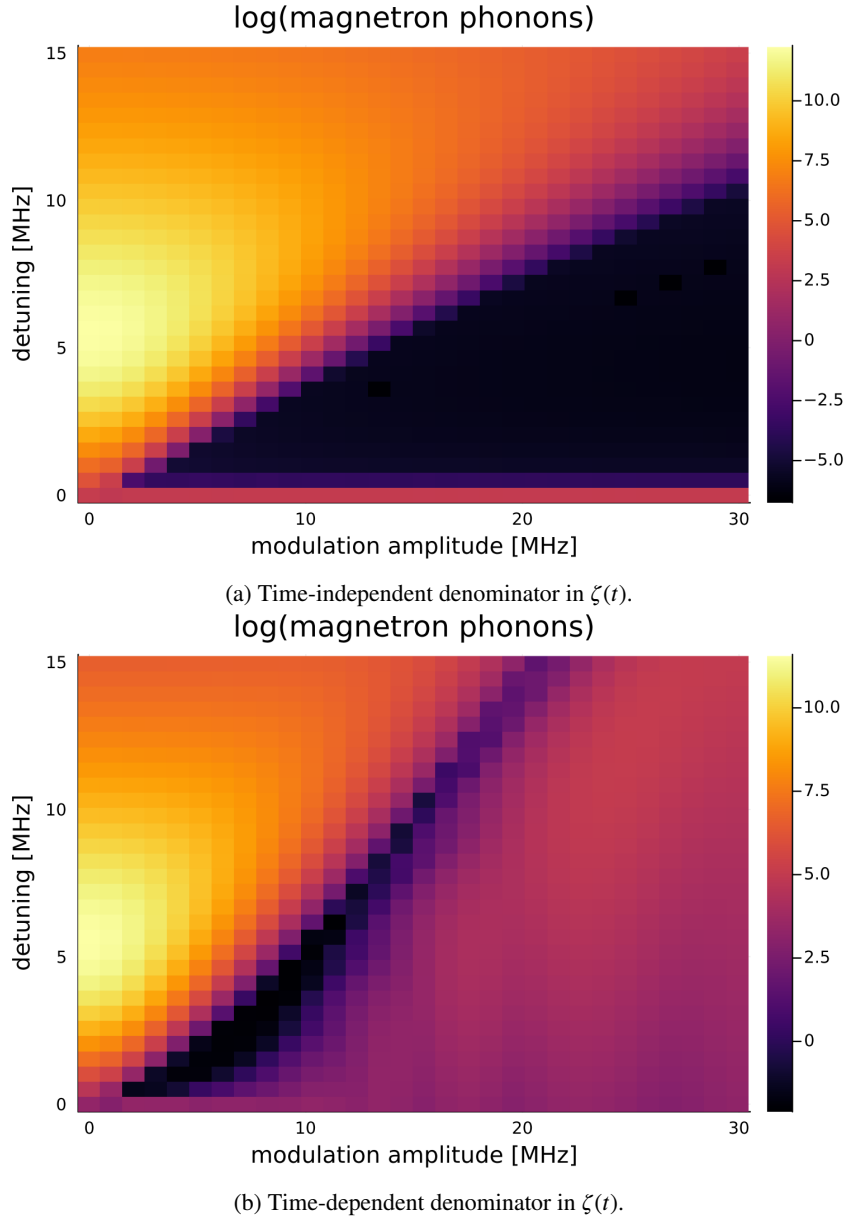


Figure 2.2: Logarithm of the number of magnetron phonons as a function of δ_0 and A_m , from 2D simulation with orthogonal beams. Parameters are: $\omega_x = 2\pi \times 2$ MHz, saturation parameter $s_0 = 0.1$, $\omega_m = 2\omega_1$. Starting conditions are 2000 magnetron phonons, 100 cyclotron phonons.

laser-ion interaction. We again see a clear cooling-heating boundary close to $2\delta_0 = A_m$. Furthermore, we note that for large A_m and relatively small δ_0 , the cooling stops working. This may be due to the aforementioned case of the amplitudes not varying slowly and the approximation consequently breaking down. Another, perhaps more physical and less mathematical, way to view it is that the λ_{\pm} (if complex) shift the rotation frequencies ω_{\pm} such that we get off-resonance if that shift is too significant. Moreover, the cooling limit is significantly higher than in the non-stochastic and linearised simulations.

To better understand these discrepancies, we need to analyse the spectrum of F_{RP} and include the fluctuation of the force exerted by the laser on the ion, which will be done in chapter 5. We can summarise that the cooling in the analytic simulation is much more robust and clean, leading to much lower average phonon numbers, which is not surprising as the laser fluctuation is neglected. Furthermore, we observe a significant dependence on the parameters δ_0 and A_m .

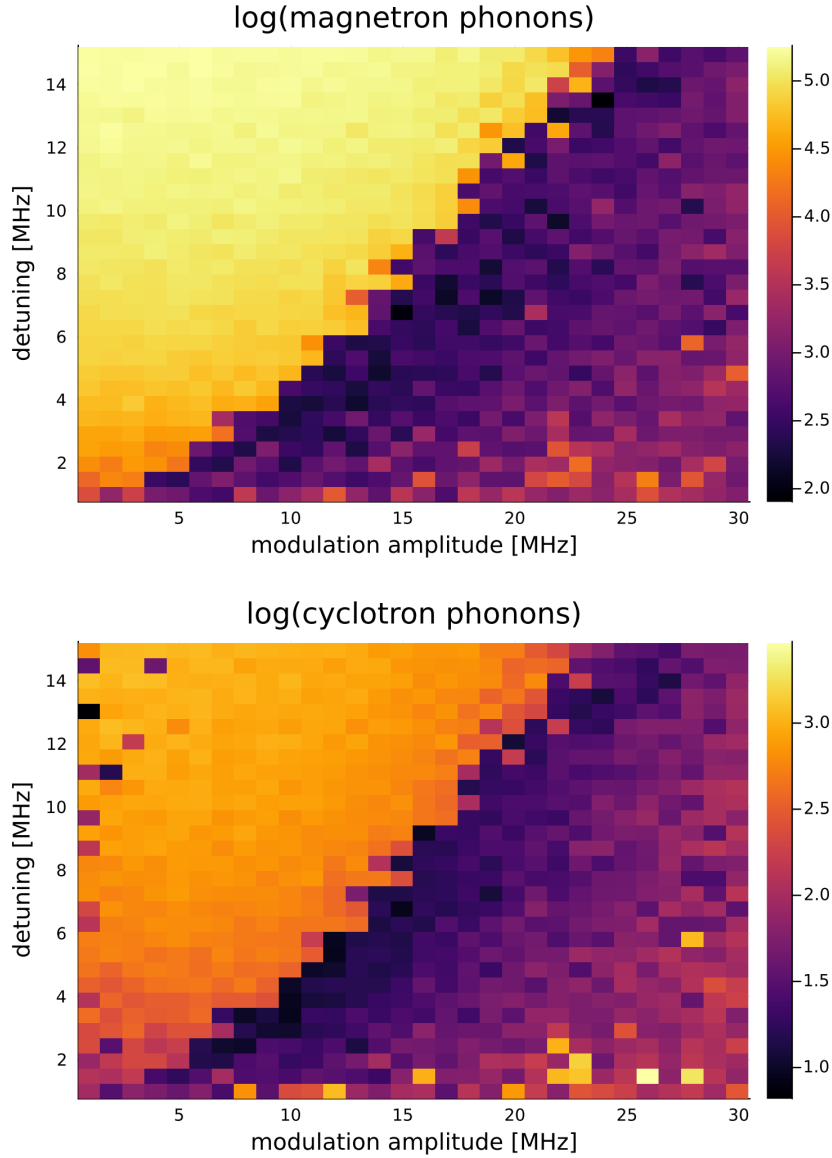


Figure 2.3: Logarithm of the number of magnetron and cyclotron phonons as a function of δ_0 and A_m , gained from 3D stochastic simulation. Parameters are: $\omega_x = 2\pi \times 2$ MHz, saturation parameter $s_0 = 0.1$, $\omega_m = 2\omega_1$. Starting conditions are 2000 magnetron phonons, 100 cyclotron phonons. Datapoints are averages over 5ms in 'steady state'.

2.4.1 Taylor Approximation in the Stochastic Simulation

Aside from the force fluctuation, the other main difference between the simulations used in figure 2.3 and 2.2b is the fact that the radiation pressure force was Taylor-approximated for small ν in the latter. To explore this difference, we can make the essentially identical approximation for the stochastic simulation (here, we approximate the scattering rate instead of the force). The result is shown in figure 2.4. We note a striking similarity to figure 2.2b. The region, where cooling occurs, is similar but the phonon numbers to which the two modes are cooled are still very different. Meanwhile, the limits found in the stochastic and Taylor-approximated model (2.4) resemble those of the non-approximated, stochastic one (2.3). Hence, to arrive at a more accurate model of the physics, we have to adapt our model in two ways. Firstly, we need to find a way to include the stochastic nature of the radiation pressure force into the treatment. Secondly, we want to extend the Taylor approximation of F_{RP} to higher order terms.

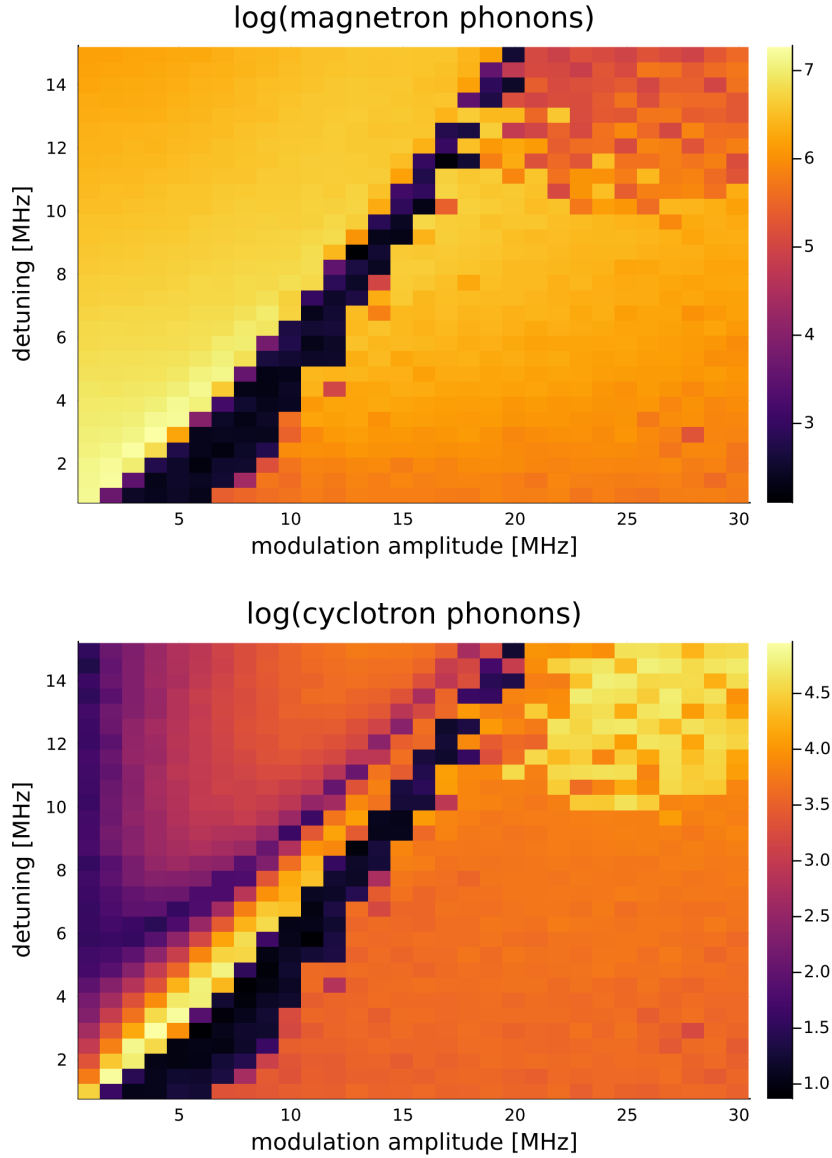


Figure 2.4: The same situation as in figure 2.3 but now with a scattering rate which is Taylor-approximated in the velocity. $\omega_x = 2\pi \times 2$ MHz, saturation parameter $s_0 = 0.1$, $\omega_m = 2\omega_1$. Starting conditions are 2000 magnetron phonons, 100 cyclotron phonons.

2.4.2 Further Procedure

We have observed how approximations cause the differences between the respective plots. However, they still remain to be understood on a quantitative level. To gain further insight, in chapter 3, we will examine the spectrum of the radiation pressure force and also analyse the phase of the magnetron and the cyclotron motion (denoted θ_{\pm} in eq. (1.8)) during the coupling. This will lead to a better understanding of the cooling mechanism. Furthermore, we will include higher orders into the Taylor expansion of the radiation pressure force. Chapters 4 and 5 will then deal with the fluctuating nature of the force.

Chapter 3

Synchronisation and Cooling Mechanism

To achieve a better understanding of the coupling mechanism, we consider the spectrum of the radiation pressure force. The dynamics of the phases of the magnetron and the cyclotron motions will be determined in order to obtain a model of the synchronisation mechanism. Then, in the next two chapters, the randomness of the force will be added to the equation.

3.1 What is coupled?

In chapter 2 we have already got an impression of the coupling mechanism. However, to get further insights, we want to revisit eq. (2.5), this time in its complex-plane formulation, which is

$$\ddot{u} + i\omega_c \dot{u} - \frac{\omega_c^2}{2} u = \Re[F_{RP}] \approx -c_0 \left(\dot{u} + \dot{\bar{u}} \right) - 2c_{m,0} \cos(\omega_m t) \left(\dot{u} + \dot{\bar{u}} \right). \quad (3.1)$$

Here, c_0 and $c_{m,0}$ are defined as the amplitude of the linearised radiation pressure force's component oscillating at 0 and ω_m , respectively, and we neglect all the other components, as they do not contribute to resonance. Looking back at the findings in chapter 2, we replace $\zeta_0 \delta_0$ and $\frac{\zeta_0 A_m}{2}$ by c_0 and $c_{m,0}$, respectively, which allows us to not make the approximation of neglecting the time dependence in the denominator (eq. (2.6)). These coefficients' units are [2 π /s] and their magnitude will be examined more thoroughly in section 3.4.

To illustrate the coupling-mechanism, it is useful to think about the RHS of eq. (3.1) in terms of its frequency-space representation, as depicted in figure 3.1. While the ion's velocity has two components oscillating at $-\omega_{\pm}$, one per motional mode, its complex conjugate rotates in the other direction, resulting in bands at $+\omega_{\pm}$. Meanwhile, the 'laser-part' of the radiation pressure force has the aforementioned three bands, one at 0 and one at $\pm\omega_m$ each (in the figure the case of $\omega_m = \omega_c$ is depicted) plus possibly others which do not contribute to resonance. Multiplying the 'velocity-part' of the linearised F_{RP} with its 'laser part' then leads to sidebands at $\pm\omega_{\pm}$ and $\pm\omega_m \pm \omega_{\pm}$, where each \pm is to be understood individually (i.e. 4+8 bands). This results in two sidebands resonant with each mode (i.e. at $-\omega_{\pm}$), one of which is proportional to c_0 and the amplitude of the respective mode and the other one of which is proportional to $c_{m,0}$ and the (c.c.) amplitude of the other mode. This resonance is where the mode-coupling comes from. As an example, for $\omega_m = \omega_c$, we get the coupling bands from $-\omega_c + \omega_{\pm}$, which is the reason why $\omega_m = \omega_c$ did not result in any cooling in the model based on eq. (2.4).

3.2 Equations for Amplitude and Phase

To increase our understanding of what happens during the interaction of the two ions with the laser, we want to treat it as a synchronisation problem, following [15]. We aim to find equations like (8.13) (in [15]), giving the time derivative of both the amplitude and phase of the ion's motion. We shall look at two different (but essentially equivalent) paths to achieve this goal.

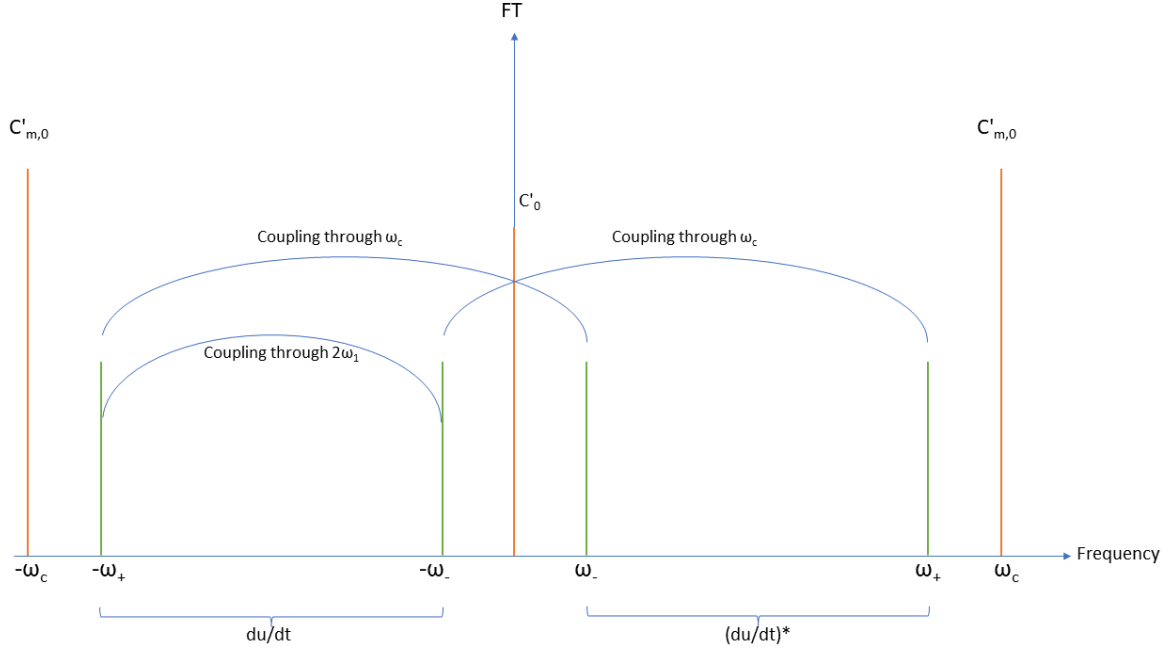


Figure 3.1: Illustration of the coupling mechanism in frequency space. Green is the ion's motion, orange is the radiation pressure force. Through F_{RP} the cyclotron and the magnetron are coupled.

3.2.1 In the rotating frame, following up on chapter 2

Starting from eq. (2.14), where we made the ansatz displayed in eq. (2.13) for the coordinate q rotating according to eq. (2.8), we can split the complex amplitudes $C(t)$ and $B(t)$ into a real radius and phase:

$$C(t) = R_- e^{i\theta_-} \quad (3.2a)$$

$$B(t) = R_+ e^{i\theta_+}. \quad (3.2b)$$

For each of the equations in eq. (2.14), we then get two equations corresponding to the real and the imaginary part, leading to the following system of equations:

$$\dot{R}_- = \frac{\zeta_0}{4\omega_1} (\omega_c \delta_0 R_- + A_m \omega_+ R_+ \cos(\theta_1)) \quad (3.3a)$$

$$\dot{\theta}_- = \frac{\zeta_0}{4\omega_1} A_m \omega_+ \frac{R_+}{R_-} \sin(\theta_1) \quad (3.3b)$$

$$\dot{R}_+ = -\frac{\zeta_0}{4\omega_1} (\omega_c \delta_0 R_+ + A_m \omega_- R_- \cos(\theta_1)) \quad (3.3c)$$

$$\dot{\theta}_+ = \frac{\zeta_0}{4\omega_1} A_m \omega_- \frac{R_-}{R_+} \sin(\theta_1), \quad (3.3d)$$

where we define $\theta_1 := \theta_+ - \theta_-$. We see that the phases are both stable if they are equal or shifted by π , but as one of the modes gets cold, the corresponding phase will start changing. By this mechanism, θ_1 will jump (or oscillate, depending on initial conditions) between 0 and π . The effect on the amplitudes is that they exchange phonons if the modulation amplitude is large enough (as in eq. (2.18)), which then leads to cooling in the back-transformed variable.

3.2.2 Starting from Zero

However, performing the coordinate transformation is not necessary for a successful derivation of the phase and amplitude dynamics. Because it may help with intuition, we shall do the same treatment without the transformation in eq. (2.8), starting from a "one beam in real direction" formulation of our system dynamics as in eq. (3.1).

We make the following ansatz for the ion's motion under the influence of the radiation pressure force:

$$u(t) = B_+(t)e^{-i\omega_+t} + B_-(t)e^{-i\omega_-t} \quad (3.4)$$

for the complex amplitudes B_\pm , which are assumed to be slowly varying ($\ddot{B}_\pm \approx 0$). This corresponds to eq. (2.13) in the rotating frame treatment. In a next step, we take further derivatives:

$$\dot{u} = \dot{B}_+e^{-i\omega_+t} - i\omega_+B_+e^{-i\omega_+t} + \dot{B}_-e^{-i\omega_-t} - i\omega_-B_-e^{-i\omega_-t} \quad (3.5a)$$

$$\ddot{u} \approx -2i\omega_+\dot{B}_+e^{-i\omega_+t} - \omega_+^2B_+e^{-i\omega_+t} - 2i\omega_-\dot{B}_-e^{-i\omega_-t} - \omega_-^2B_-e^{-i\omega_-t} \quad (3.5b)$$

Inserting these into eq. (3.1) we can find two resonant equations of interest, one each with factor $e^{-i\omega_\pm}$:

$$-2i\omega_\pm\dot{B}_\pm - \omega_\pm^2B_\pm + i\omega_c(\dot{B}_\pm - i\omega_\pm B_\pm) - \frac{\omega_z^2}{2}B_\pm = -c_0(\dot{B}_\mp - i\omega_\mp B_\mp) - 2c_{m,0}(\dot{B}_\mp - i\omega_\mp B_\mp), \quad (3.6)$$

which can be simplified to read

$$-2i\omega_\pm\dot{B}_\pm + i\omega_c\dot{B}_\pm = -c_0(\dot{B}_\mp - i\omega_\mp B_\mp) - 2c_{m,0}(\dot{B}_\mp - i\omega_\mp B_\mp). \quad (3.7)$$

Now, we want to find equations describing the dynamics of the phase and the real part of the amplitude again, so we split the complex variables into two real ones:

$$B_\pm = R_\pm e^{i\theta_\pm}. \quad (3.8)$$

Inserting these into eq. (3.7) and committing to $\omega_m = \omega_c$ (the case of $\omega_m = 2\omega_1$ can be treated analogously), we attain

$$(\dot{R}_\pm + iR_\pm\dot{\theta}_\pm)(\mp i2\omega_1 + c_0) - ic_0\omega_\pm R_\pm = -2c_{m,0}(\dot{R}_\mp - iR_\mp\dot{\theta}_\mp + i\omega_\mp R_\mp), \quad (3.9)$$

oscillating at $-\omega_\pm$ respectively. Again, each equation can be split into real and imaginary parts, leading to 4 equations which we can solve for \dot{R}_\pm and $\dot{\theta}_\pm$.

The result does not yet look as presentable as eq.s (3.3), but in the low laser power limit $c_0, c_{m,0} \ll \omega_1, \omega_-$ (as long as the axial frequency does not grow too large, e.g. $\omega_x \lesssim 3$ MHz) and we, therefore, can neglect some of the terms, $\frac{c_{(m),0}}{\omega_{1,-}} \approx 0$, which leads to the more readable expressions

$$\dot{R}_- = \frac{1}{2\omega_1} (c_0\omega_-R_- - c_{m,0}\omega_+R_+ \cos(\theta_c)) \quad (3.10a)$$

$$\dot{\theta}_- = \frac{1}{2\omega_1} c_{m,0}\omega_+ \frac{R_+}{R_-} \sin(\theta_c) \quad (3.10b)$$

$$\dot{R}_+ = \frac{1}{2\omega_1} (-c_0\omega_+R_+ + c_{m,0}\omega_-R_- \cos(\theta_c)) \quad (3.10c)$$

$$\dot{\theta}_+ = -\frac{1}{2\omega_1} c_{m,0}\omega_- \frac{R_-}{R_+} \sin(\theta_c), \quad (3.10d)$$

where we define $\theta_c := \theta_+ + \theta_-$.

These expressions are similar to eq.s (3.3), but here the asymmetry in the heating and cooling rates is contained in the equations as we use a non-transformed frame. The said asymmetry, namely the fact that the c_0 -band cools

the cyclotron stronger than it heats the magnetron mode, is the basis of the cooling mechanism. If it were not asymmetric, we would only get a phonon exchange and no net cooling. Similarly, if the magnetron mode was heated faster than the cyclotron is cooled, we would need blue detuning for net cooling.

Furthermore, we notice that the phases only appear as θ_c and, consequently, we can reduce the number of equations by one, so we arrive at the following dynamics for the phases:

$$\dot{\theta}_c = \frac{1}{2\omega_1} c_{m,0} \sin(\theta_c) \left(\omega_+ \frac{R_+}{R_-} - \omega_- \frac{R_-}{R_+} \right). \quad (3.11)$$

It follows that the sum of the phases will be relatively stable around 0 or π , but will change once one of the amplitudes becomes very small. Again, this results in a phonon exchange between the two motional modes, where θ_c determines which mode is being cooled and which one is being heated.

3.2.3 Cooling Condition Revisited

Before decomposing the complex amplitudes B_{\pm} into two real numbers, the dynamics described by eq. (3.7) can be summarized in a matrix form to read

$$\frac{d}{dt} \begin{bmatrix} B_+(t) \\ B_-(t) \end{bmatrix} = \frac{1}{2\omega_1} \begin{bmatrix} -c_0\omega_+ & -c_{m,0}\omega_- \\ c_{m,0}\omega_+ & c_0\omega_- \end{bmatrix} \times \begin{bmatrix} B_+(t) \\ B_-(t) \end{bmatrix}, \quad (3.12)$$

where we commit to $\omega_m = 2\omega_1$. Realising that we observe the cooling of both modes if and only if both eigenvalues of this matrix have a negative real part, we arrive at a band-strength version of the cooling condition presented in eq. (2.18). The eigenvalues can straightforwardly be extracted and we obtain

$$0 < c_0 < c_{m,0}, \quad (3.13)$$

as the condition for cooling in the model of a linearised radiation pressure force.

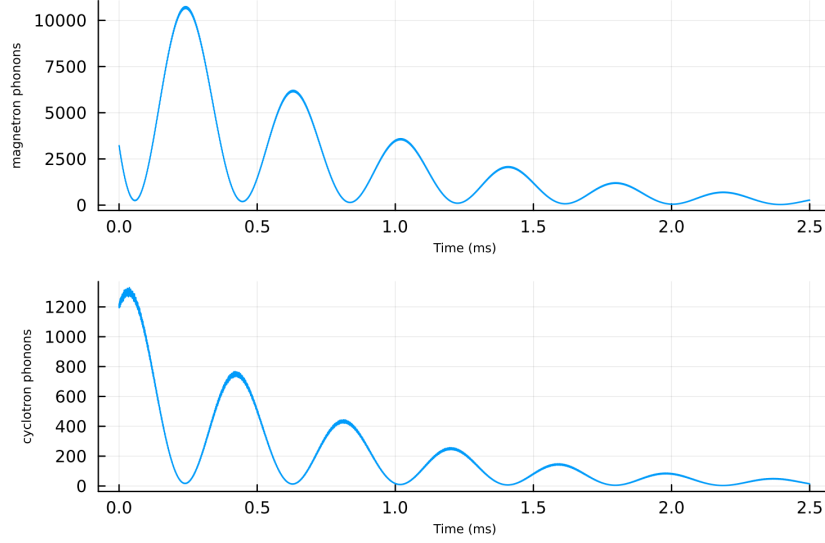
3.3 Visualisation of the Phase and Amplitude Trajectory

To check the quality of the calculations, the result is compared to the simulation of the system described in eq. (2.5) which is depicted in figure 3.2. Here, on top of the energy over time, the phase was extracted from the simulation by fitting eq.s (1.8) to the ion position and velocity with fitting-parameter θ_{\pm} . We can see that θ_c is relatively stable as it approaches 0 or π , where the former case coincides with the magnetron mode being cooled, while the latter appears when it heats up. Then, as one of the modes gets cold, θ_c drifts until it approaches a stable region once more. This is precisely what is described by eq.s (3.10).

3.4 Spectrum Analysis of the Radiation Pressure Force

To develop a quantitative sense for c_0 and $c_{m,0}$ as a function of the detuning and the modulation amplitude, we want to analyse the spectrum of the linearised radiation pressure force. More specifically, the Fourier transform of the linear term, $\zeta(t)$ as in eq. (2.3), is taken, where, amongst others, peaks appear at the frequencies 0 and ω_m . These are the relevant ‘resonant bands’ which lead to frequency modulation cooling, as illustrated in figure 3.1. To finally find the coefficients, the rest of the spectrum is set to zero and the inverse Fourier transform is taken.

The result is shown in fig. 3.3. It is immediately noticeable that for large A_m , the non-oscillating band’s strength, c_0 , becomes negative. This corresponds to a blue detuning and according to eq. (3.13) no cooling is expected in these regions. Meanwhile, the strength of the oscillating band $c_{m,0}$ on its own is not very informative, but comparing it to the strength of the detuning band, we find that for large detunings $c_{m,0} < c_0$, another violation



(a) Phonons over time in both modes.

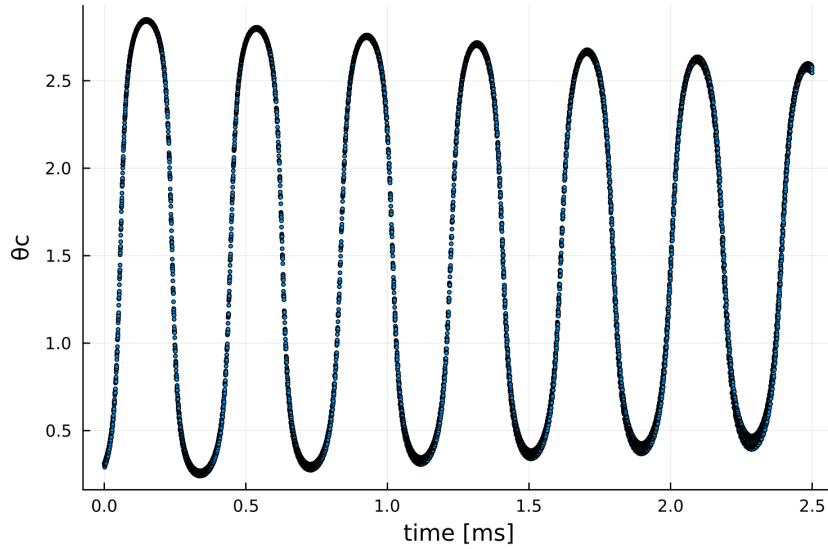

 (b) The corresponding ' θ_c '.

Figure 3.2: Simulation of phonons and phase as function of time, based on eq. (2.5), for coefficients $\omega_m = \omega_c$, $A_m = 2\pi \times 18$ MHz, $\delta_0 = 2\pi \times 10$ MHz, $s = 0.5$. Depending on θ_c , either the cyclotron or the magnetron mode is cooled.

of the the cooling condition (3.13), is encountered. The combination explains why cooling can be observed only in this specific region in fig.s 2.2b and 2.4. This will be illustrated in a more processed way in figure 5.3.

3.5 Higher Order Taylor Approximation

We have seen in chapter 2 that the linearisation of the radiation pressure force is only justified to a certain extent. To get closer to the full expression, as described in eq. (2.1), we want to include higher orders in the Taylor approximation, and add them in eq. (3.1). Then, we can essentially repeat the treatment of section 3.2.2. We shall stick to modulation at $\omega_m = 2\omega_1$, but the case of $\omega_m = \omega_c$ can, of course, be treated analogously.

The second order Taylor expansion does not yield any new relevant resonant terms, as a spectrum analysis shows. However, in the third order expansion, indeed new resonant bands appear at the frequencies $0, \pm 2\omega_1$ and $\pm 4\omega_1$ and we shall denote their respective strengths $\frac{c_{30}}{3}, \frac{c_{31}}{3}$ and $\frac{c_{32}}{3}$. Again sticking to the regime of weak laser

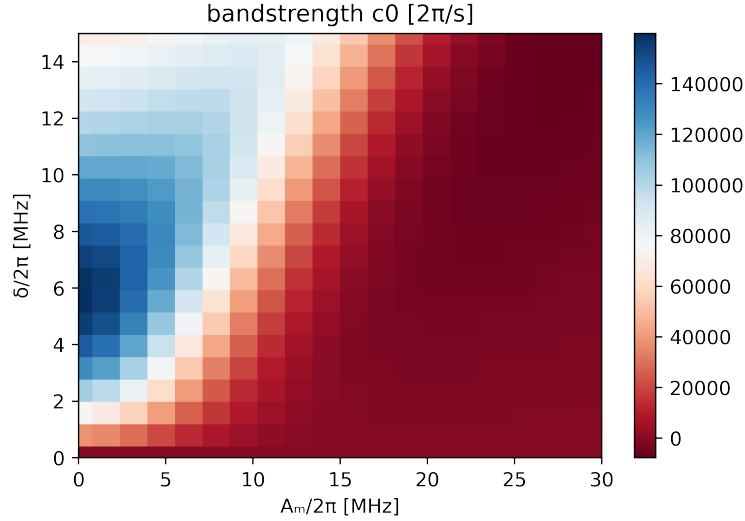
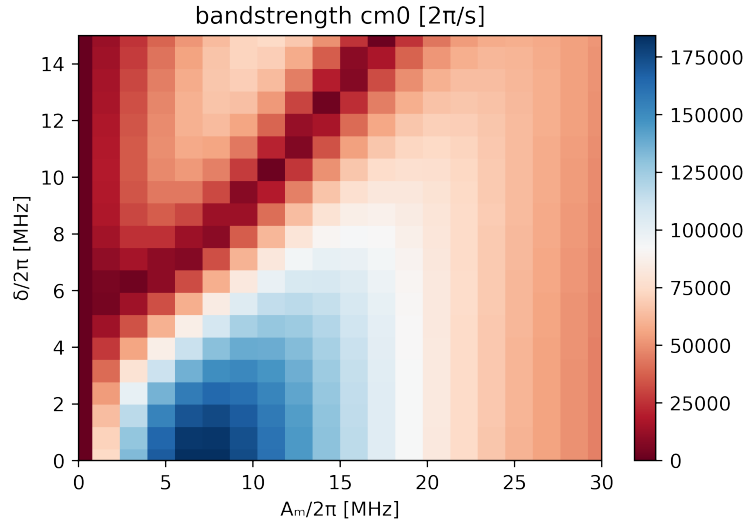

 (a) The numerical value of c_0 as a function of δ_0 and A_m .

 (b) The numerical value of $c_{m,0}$ as a function of δ_0 and A_m .

 Figure 3.3: Bandstrengths as a function of detuning and modulation amplitude for 2 MHz trapfrequency and 0.1 intensity saturation. For large A_m we observe that $c_0 < 0$ and comparing the two we can find the region in which the cooling condition (3.13) is fulfilled.

power, i.e. small coefficients c_i compared to the trap frequencies, we then arrive at the time derivative of the complex amplitudes

$$\mp i 2\omega_1 \dot{B}_\pm = -(c_0 + 2c_{m,0} \cos 2\omega_1 t)(\dot{u} + \ddot{u}) + \frac{1}{3}(c_{30} + 2c_{31} \cos 2\omega_1 t + 2c_{32} \cos 4\omega_1 t)(\dot{u} + \ddot{u})^3|_{-\omega_\pm}, \quad (3.14)$$

where on the RHS we select the terms oscillating at $-\omega_\pm$, which are resonant with the motion. Now, we can insert $\dot{u} \approx -iB_+\omega_+e^{-i\omega_+t} - iB_-\omega_-e^{-i\omega_-t}$. The two equations that arise from this are

$$\mp \frac{2\omega_1}{\omega_\pm} \dot{C}_\pm = c_0 C_\pm + c_{m,0} C_\mp - c_{30}(|C_+|^2 + |C_-|^2)C_\pm - c_{31} \left((|C_+|^2 + |C_-|^2)C_\mp + C_\pm^2 C_\mp^* \right) - c_{32} C_\mp^2 C_\pm^*, \quad (3.15)$$

where, for notation purposes, we define $C_\pm := B_\pm \omega_\pm$.

Unsurprisingly, we can conclude that for small radii, i.e. relatively cold ions, the linearisation of the radiation

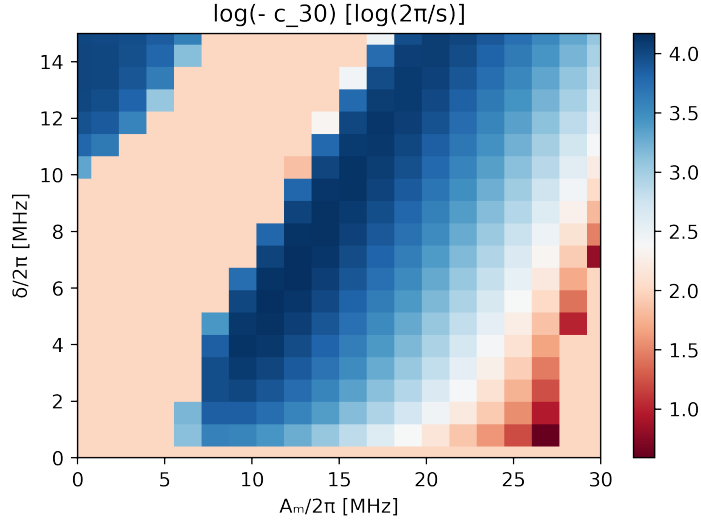


Figure 3.4: The logarithm of $-c_{30}$ as a function of detuning and modulation amplitude. Where $c_{30} > 0$, the bandstrength was set to -100.

pressure force seems to be justified, while for hotter ions the importance of the third order Taylor terms increases. While the effect of the third order coupling terms is not entirely clear, we can combine the two non-coupling terms (which we shall call ‘self-sufficient’ in the future) into a single, radius-dependent one as follows:

$$\mp \frac{2\omega_1}{\omega_{\pm}} \dot{C}_{\pm} = \tilde{c}_0(|C_+|^2, |C_-|^2) C_{\pm} + c_{m,0} C_{\mp} - c_{31} \left((|C_+|^2 + |C_-|^2) C_{\mp} + C_{\pm}^2 C_{\mp}^* \right) - c_{32} C_{\mp}^2 C_{\pm}^*. \quad (3.16)$$

Hence, the effect of the third order Taylor approximation is, amongst others, a correction to c_0 , which depends on the temperature of the mode.

Another way to achieve more insights is by repeating the follow-up treatment done in section 3.2.2 i.e. dissecting the complex amplitudes B_{\pm} into two real numbers, namely a phase and an amplitude as in eq. (3.8). The resulting expression then yields four real equations which can be solved for \dot{R}_{\pm} and $\dot{\theta}_{\pm}$:

$$\dot{\theta}_{\pm} = \frac{R_{\mp} \omega_{\mp}}{2\omega_1 R_{\pm}} \sin \theta_1 \left(-c_{m,0} + c_{31} R_{\mp}^2 \omega_{\mp}^2 + 2c_{32} R_+ R_- \omega_+ \omega_- \cos \theta_1 \right) \quad (3.17a)$$

$$2\omega_1 \dot{R}_{\pm} = \mp c_0 R_{\pm} \omega_{\pm} \pm c_{30} R_{\pm}^3 \omega_{\pm}^3 \pm R_{\mp} \omega_{\mp} \left((-c_{m,0} + c_{31} R_{\mp}^2 \omega_{\mp}^2 + 2c_{31} R_{\pm}^2 \omega_{\pm}^2) \cos \theta_1 + c_{32} R_- R_+ \omega_- \omega_+ \cos 2\theta_1 \right) \quad (3.17b)$$

where we define $\theta_1 := \theta_- - \theta_+$.

In eq. (3.17b) we see that the sign of the third Taylor order non-oscillating band’s coefficient, c_{30} , is flipped, compared to the first order’s, c_0 . Hence, we need a negative c_{30} for the ion to experience the effect a red detuning would have, which is cooling the cyclotron while heating the magnetron mode. If c_{30} acts as a red detuning, this will, for large R_{\pm} , compensate for the blueness of c_0 , which appears in certain regions, as discussed in section 3.4. The logarithm of $-c_{30}$ as a function of detuning and modulation amplitude is displayed in figure 3.4. Indeed, in the regions where cooling was observed in the non-approximated laser-ion interaction (shown in 2.3), but heating was encountered in the linearised model (as in 2.4) we find a red, i.e. negative, bandstrength c_{30} . This provides a qualitative explanation for the discrepancy between figures 2.3 and 2.4.

Now that we have established a solid understanding of the cooling process in the absence of force fluctuations, we seek to expand our investigation to cases in which they are in fact present.

Chapter 4

The Cooling Rate

So far, we have treated the force exerted by the laser and experienced by the ion as its average, i.e. the radiation pressure force:

$$F_l(t, \mathbf{v}) \approx F_{RP}(t, \mathbf{v}) = \langle F_l(t, \mathbf{v}) \rangle, \quad (4.1)$$

where the expectation value denotes an ensemble average, i.e. an average over a cloud of non-interacting ions. In this chapter, we want to stop making this approximation and treat the force exerted by the light for what it is:

$$F_l(t, \mathbf{v}) = F_{RP}(t, \mathbf{v}) + F'_{RP}(t, \mathbf{v}), \quad (4.2)$$

where F'_{RP} represents the fluctuations, invoked by the stochastic nature of photon absorption and emission and $\langle F'_{RP} \rangle = 0$. As we have investigated the cooling mechanism in chapters 2 and 3 already, we will focus on the cooling rate in this chapter before turning to the cooling limit in chapter 5.

4.1 Mathematics

To find an analytical description for the time evolution of the phonons in the radial motional modes, we follow the approach of [11] (section 3). Only the radial modes shall be considered, but the analysis can be extended to include the axial mode. Without loss of generality, we assume our laser to point along the x-axis.

The idea is to find an expression for the change in the magnetron and the cyclotron radius squared, Δr_{\pm}^2 , that an ion experiences due to a photon scattering event, which is assumed to be instantaneous. If we then multiply Δr_{\pm}^2 by the rate of scattering events, γ_s , this effectively yields a time derivative $\frac{\Delta r_{\pm}^2}{\Delta t} \approx \frac{dr_{\pm}^2}{dt}$.

To address the randomness of the scattering, we want to take an ensemble average. More specifically, the emitted photon's wavevector is stochastic and, therefore, the ion's position and velocity are of that nature as well. Mathematically, this means that we describe the ion's position as in eq.s (1.8) and average over r_{\pm} , θ_{\pm} and the emitted photon's wavevector \mathbf{k}_s . We will assume that the emission is isotropic.

Finally, we will attain expressions for the time derivative of the radii squared in the ensemble average, $\frac{d\langle r_{\pm}^2 \rangle}{dt}$, which correspond directly to the time derivative of the phonon numbers via eq. (1.10).

4.1.1 The Change in Radii Squared: Δr_{\pm}^2

As an ion moves as described in (1.8), it absorbs a photon with wavevector $\mathbf{k} = k\mathbf{e}_x$ (wlog assuming that the beam points in \bar{x} -direction) at time t and 'instantaneously' emits a photon with wavevector \mathbf{k}_s . This leads to a change in velocity of $\Delta \mathbf{v} = \hbar(\mathbf{k} - \mathbf{k}_s)$. To find the change in radii squared, we then need the expression for the radius

before the scattering event, which is given by eq. (1.11), but also after it:

$$(r'_{\pm})^2 = \frac{1}{4\omega_1^2} \left((\omega_{\mp}x + \dot{y} + \Delta v_y)^2 + (\omega_{\mp}y - \dot{x} - \Delta v_x)^2 \right). \quad (4.3)$$

The changes in radii squared are then given by $(r'_{\pm})^2 - r_{\pm}^2$, which evaluates to

$$\Delta r_{\pm}^2 = \frac{(\Delta v_x)^2 + (\Delta v_y)^2}{4\omega_1} \mp \frac{r_{\pm}}{\omega_1} \left[\sin(\omega_{\pm}t + \theta_{\pm})\Delta v_x + \cos(\omega_{\pm}t + \theta_{\pm})\Delta v_y \right]. \quad (4.4)$$

4.1.2 The Scattering Rate: γ_s

The scattering rate of a beam with intensity I and wavenumber $k = \frac{\omega}{c}$, hitting an ion with cross section σ is

$$\gamma_s = \frac{I}{\hbar\omega} \sigma(\delta(t), \mathbf{v}), \quad (4.5)$$

where the wavevector undergoes negligible fluctuations over time $k(t) \approx k$. The scattering cross-section can, for small velocities, be Taylor-approximated

$$\sigma(\delta(t), \mathbf{v}) = \frac{\sigma_0 \Gamma^2}{4} \frac{1}{(\delta(t) + \mathbf{k} \cdot \mathbf{v})^2 + \frac{\Gamma^2}{4}} \approx \frac{\sigma_0 \Gamma^2}{4} \left(\frac{1}{\delta(t)^2 + \frac{\Gamma^2}{4}} - \frac{2\delta(t)\mathbf{k} \cdot \mathbf{v}}{\left(\delta(t)^2 + \frac{\Gamma^2}{4}\right)^2} \right), \quad (4.6)$$

where Γ is the decay rate and $\sigma_0 = \frac{2\pi}{k^2}$ is a constant. Through the frequency modulation that we are applying, the detuning becomes time-dependent, as described in eq. (1.14).

4.1.3 Multiplying and Averaging over the Ensemble

Now that we know where to start, we can begin the calculation by multiplying eq.s (4.5) and (4.4) and then take the ensemble average of the resulting expression. The first fraction in eq. (4.4), when multiplied by the scattering rate, amounts to a time-varying heating rate when averaged over the ensemble

$$h(t) := \langle \gamma_s \rangle_{\theta} \left(\frac{\hbar k}{2m\omega_1} \right)^2 (1 + f_{sx} + f_{sy}), \quad (4.7)$$

where

$$f_{si} = \int P(\hat{\mathbf{k}}_s) \hat{\mathbf{k}}_{s,i}^2 d\Omega \quad (4.8)$$

is a coefficient describing how much the emission of a photon affects direction i . Furthermore, the ensemble average over the scattering rate simply yields $\langle \gamma_s \rangle_{\theta} = \gamma_s(t, \mathbf{v} = 0)$.

Before delving into addressing the remaining matters of multiplying eq. (4.4) by eq. (4.5), we note that, assuming isotropic emission

$$\langle \Delta v_x \rangle_{\mathbf{k}_s} = \frac{\hbar k}{m} \quad (4.9a)$$

$$\langle \Delta v_y \rangle_{\mathbf{k}_s} = 0, \quad (4.9b)$$

and as these terms are the only ones being averaged over the wavenumber of the emitted photon, the last term in eq. (4.4) always averages to zero, also when multiplied by γ_s . To further tidy up the calculation, we shall define

$$\alpha := \frac{I \langle \Delta v_x \rangle \sigma_0 \Gamma^2}{4\hbar\omega\omega_1} = \frac{I \sigma_0 \Gamma^2}{4mc\omega_1}, \quad (4.10)$$

collecting all the dynamically not interesting coefficients. Accordingly, in order to promptly regain a comprehensive

overview of our current status: Starting from eq.s (4.4) and (4.5), we arrived at

$$\frac{d \langle r_{\pm}^2 \rangle}{dt} = h(t) \mp \alpha \left\langle \left(\frac{1}{\delta(t)^2 + \frac{\Gamma^2}{4}} - \frac{2\delta(t)k v_x}{\left(\delta(t)^2 + \frac{\Gamma^2}{4}\right)^2} \right) \frac{r_{\pm}}{\omega_1} \sin(\omega_{\pm} t + \theta_{\pm}) \right\rangle, \quad (4.11)$$

and the first term in the bracket will clearly average to zero, assuming that our phases are evenly distributed, i.e. $P(\theta_{\pm}) = \text{const}$. Eq.s (3.10) support this assumption, while they imply that the motional phases are correlated, $P(\theta_+, \theta_-) \neq \text{const}$, which will be discussed in the following sections of this chapter.

For further evaluating eq. (4.11), an expression for the ion's velocity in the x-coordinate can be derived from eq. (1.8), to yield

$$v_x = -r_- \omega_- \sin(\omega_- t + \theta_-) - r_+ \omega_+ \sin(\omega_+ t + \theta_+). \quad (4.12)$$

By consecutively inserting this and averaging the arising \sin^2 -term over the respective phase, we find that

$$\frac{d \langle r_{\pm}^2 \rangle}{dt} = h(t) \mp \alpha \left\langle \frac{2\delta(t)k r_{\pm}}{\left(\delta(t)^2 + \frac{\Gamma^2}{4}\right)^2} \left(r_{\mp} \omega_{\mp} \sin(\omega_{\pm} t + \theta_{\pm}) \sin(\omega_{\mp} t + \theta_{\mp}) + \frac{r_{\pm} \omega_{\pm}}{2} \right) \right\rangle, \quad (4.13)$$

which we then want to rearrange such that we arrive at a coupling, $\propto \langle r_+ r_- \rangle$, and a 'self-sufficient', $\propto \langle r_{\pm}^2 \rangle$, term:

$$\frac{d \langle r_{\pm}^2 \rangle}{dt} = h(t) \mp \frac{2\delta(t)k\alpha}{\left(\delta(t)^2 + \frac{\Gamma^2}{4}\right)^2} \left(\langle r_+ r_- \rangle \omega_{\mp} \langle \sin(\omega_+ t + \theta_+) \sin(\omega_- t + \theta_-) \rangle + \frac{\langle r_{\pm}^2 \rangle \omega_{\pm}}{2} \right). \quad (4.14)$$

While the coupling term is a bit more difficult to analyse, the self-sufficient term's secrets can rapidly be disclosed, if we think about a time-average which makes the quickly-oscillating terms disappear. As motivated in the context of c_0 and $c_{m,0}$ in eq. (3.1), we can re-express

$$\frac{\delta(t)}{\left(\delta(t)^2 + \frac{\Gamma^2}{4}\right)^2} \approx \tilde{c}_0 + 2\tilde{c}_{m,0} \cos \omega_m t, \quad (4.15)$$

again neglecting the off-resonant terms. Then, since $\alpha > 0$, the self-sufficient term will make the cyclotron (magnetron) mode exponentially decay (grow) and the cooling (heating) rate is $\tilde{c}_0 k \alpha \omega_{\pm}$. Thus, as already seen in eq. (3.10), the cyclotron's motional amplitude decays faster than the magnetron's grows and we can achieve a net cooling as long as we are red-detuned, $\tilde{c}_0 > 0$, and the coupling between the two modes is strong enough.

4.1.4 The coupling term

To understand the coupling term in equation (4.14), we must find a strategy to address

$$\langle \sin(\omega_+ t + \theta_+) \sin(\omega_- t + \theta_-) \rangle_{\theta} = \frac{1}{2} \langle (\cos(2\omega_1 t + \theta_1) - \cos(\omega_c t + \theta_c)) \rangle_{\theta}, \quad (4.16)$$

where we used trigonometric identities. At first glance, it is tempting to assume that this equation will average to zero, according to our assumption of constant marginals of $P(\theta_+, \theta_-)$. However, constant marginals of course do not imply that the distribution itself is constant as well. Judging from eq.s (3.10), we would assume that (for $\omega_m = \omega_c$) the sum of the phases θ_c would be more stable around 0 or π , which is also supported by figure 3.2

In that case, the two phases, θ_{\pm} are actually correlated, and, consequently, the average does not amount to zero after all. For example, if we achieved 'perfect locking', i.e. $\theta_c = \phi_{lock}(t, r_+, r_-)$ whose dynamics follow eq. (3.11), the probability distribution of θ_{\pm} would be a Dirac function $P(\theta_+, \theta_-) = \delta(\theta_+ - \theta_- - \phi_{lock})$ and it would follow

that

$$\langle (\cos(2\omega_1 t + \theta_1) - \cos(\omega_c t + \theta_c)) \rangle_\theta = \pm \cos(\omega_m t + \phi_{lock}), \quad (4.17)$$

where the sign depends on the modulation frequency. Due to stochastic fluctuation in the force, it can be expected that the locking is not perfect, i.e. θ_c is just distributed around ϕ_{lock} . In that case, the ensemble average should result in roughly the same cosine-shaped oscillation but with reduced amplitude $|A_l| \leq 1$, where $A_l < 0$ if we modulate at ω_c . Finally, we arrive at

$$\frac{d \langle r_\pm^2 \rangle}{dt} \Big|_t = h(t) \mp \frac{\delta(t) k \alpha}{\left(\delta(t)^2 + \frac{\Gamma^2}{4} \right)^2} \left(\omega_\pm \langle r_\pm^2 \rangle + \omega_\mp \langle r_+ r_- \rangle A_l \cos(\omega_m t + \phi_{lock}) \right), \quad (4.18)$$

where we note that, after averaging out quickly rotating terms, the coupling term is

$$2\tilde{c}_{m,0} \cos(\omega_{mod} t) \cos(\omega_{mod} t + \phi_{lock}) k \alpha \omega_\pm A_l \langle r_+ r_- \rangle, \quad (4.19)$$

so depending on ϕ_{lock} we will couple energy into or out of the respective mode. This is in accordance with chapter 3, but to check if it withstands the test of the fluctuating force, we will compare the result to the simulation that considers the stochastic nature of the problem in the next section. For $\omega_m = \omega_c$, assuming that the detuning and the modulation amplitude are set appropriately, both modes can be cooled for

$$\theta_c \approx 0, \quad (4.20)$$

while for $\omega_m = 2\omega_1$, we require that

$$\theta_1 \approx \pi. \quad (4.21)$$

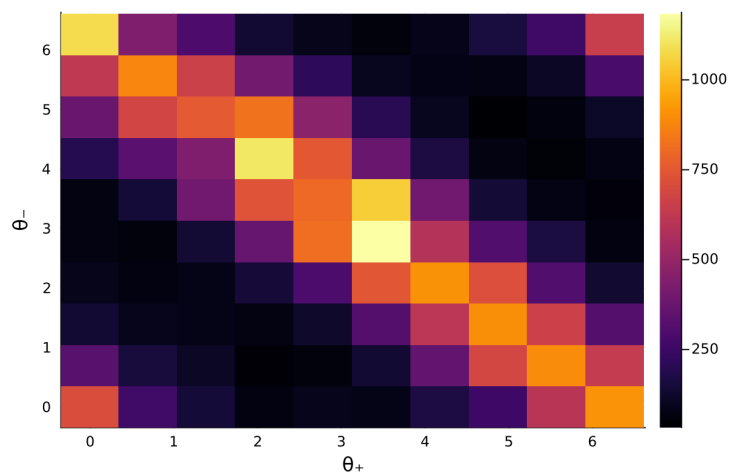
As in chapter 3, we have seen that the frequency modulation couples the two modes of motion and the cooling effect is invoked because the red-detuned cooling beam sucks more energy out of the cyclotron mode than it puts into the magnetron mode. On a shorter timescale, the energy exchange is mediated by θ_c or θ_1 , which follows the dynamics found in eq.s (3.10), but also underlies the force fluctuations.

4.2 Visualisation of Synchronisation under a Stochastic force

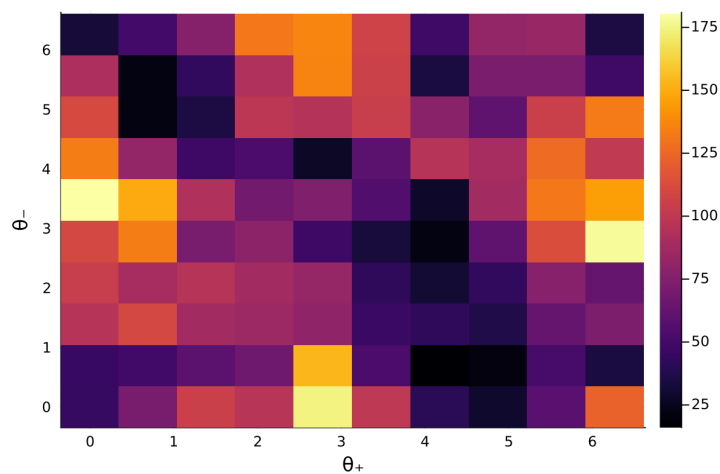
To see how the force fluctuations affect the phase and, thereby, the cooling rate, we want to extract the phases from the stochastic simulation as we already did for the mean-force simulation in figure 3.2. However, we should also keep in mind that in these simulations the full, non-linearised version of the scattering cross section is used (i.e. the approximation in eq. (4.6) is not made).

4.2.1 The relation between θ_+ and θ_-

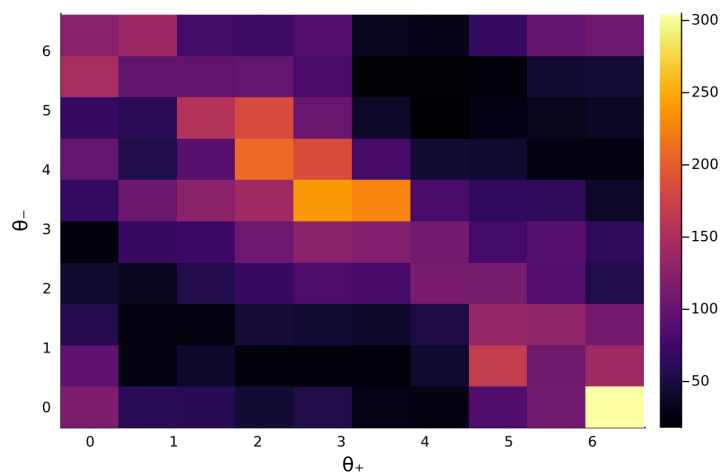
For $\omega_m = \omega_c$, we expect to see the magnetron mode to be cooling only if $\theta_c \approx 0$, according to eq.s (3.10) and (4.18), and the same applies to the heating of the cyclotron mode. To check that this also holds in the presence of a fluctuating force, the phases were extracted from a phonons-over-time plot and compared to the gradient of the phonon number, as presented in figure 4.1. We can observe that the magnetron mode's cooling coincides with $\theta_c \approx 0$, which also holds for the cyclotron heating. These findings agree with the rate equations (4.18), which suggest that the only way the magnetron is cooled and the cyclotron is heated, is through the mode-coupling for said $\theta_c \approx 0$. Meanwhile, the counts for the magnetron mode's heating are more randomly distributed, but there is fewer straying around $\theta_c \approx 0$. This can be explained analogously with the difference that the magnetron experiences heating not only through the coupling when $\theta_c \approx \pi$ but also through the self-sufficient, $\propto \tilde{c}_0 \langle r_-^2 \rangle$, term.



(a) Relation for $\frac{dn_-}{dt} < 0$.

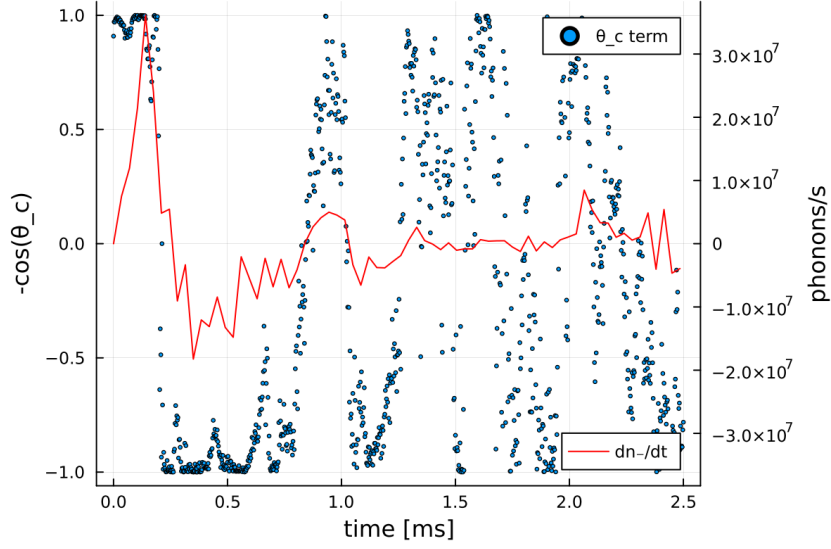
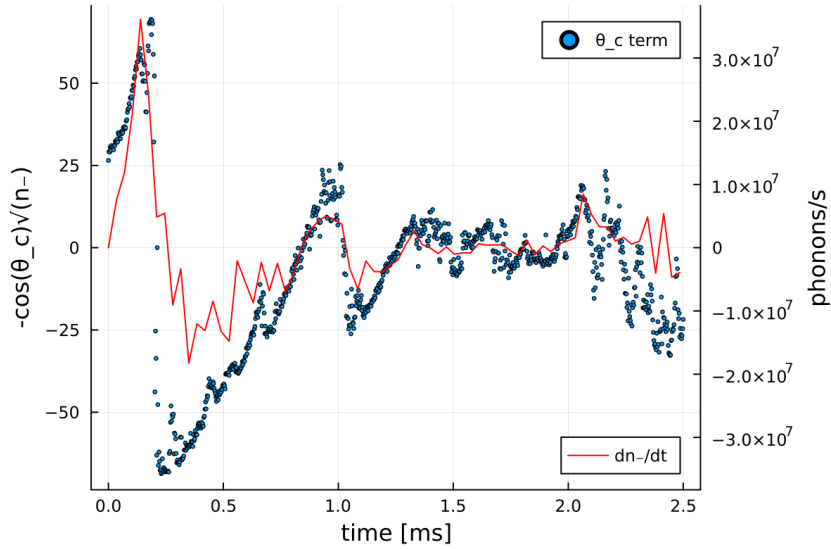


(b) Relation for $\frac{dn_+}{dt} > 0$.



(c) Relation for $\frac{dn_+}{dt} > 0$.

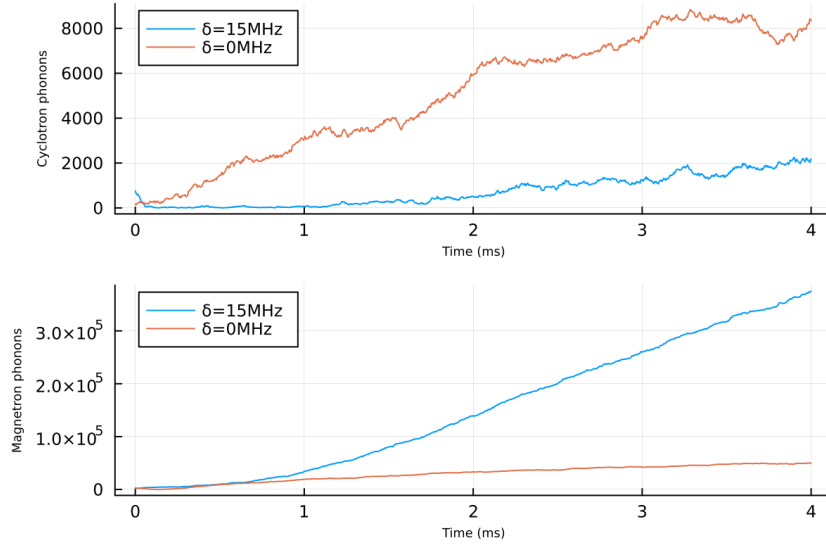
Figure 4.1: Relation of θ_{\pm} at $\omega_m = \omega_c$, $A_m = 2\pi \times 22$ MHz, $\delta_0 = 2\pi \times 10$ MHz, $s_0 = 0.5$, where datapoints are selected according to whether the modes are heating or cooling. The colours indicate the number of incidents counted.

4.2.2 The Relation Between θ_c and n_- (a) Comparison of $-\cos(\theta_c)$ and $\frac{dn_-}{dt}$.(b) Comparison of $-\cos(\theta_c)\sqrt{n_-}$ and $\frac{dn_-}{dt}$, for scaling.Figure 4.2: Visualisation of the correlation between θ_c and the time derivative in magnetron phonons. $A_m = 2\pi \times 20$ MHz, $\delta_0 = 2\pi \times 6$ MHz, $s_0 = 0.1$.

In figure 4.2, the effect the coupling term has on the the time derivative of the magnetron phonon number is further illustrated. By studying figure 4.2a, we see that the magnetron mode cooling, i.e. $\dot{n}_- < 0$ coincides with $-\cos\theta_c < 0$, especially at the beginning of the cooling cycle when both modes are relatively hot.

To improve the visual effect of the plot, $-\cos(\theta_c)$ is multiplied by a factor of $\sqrt{n_-}$ for figure 4.2b, i.e. we rescale the cos-term by one of the factors appearing alongside it in eq. (4.18) (heuristically relating $\langle r_+ r_- \rangle \simeq \sqrt{n_+ n_-}$). Our observation indicates that the curves exhibit a high degree of conformity when the modes have a relatively high temperature. Once they are cold, the synchronisation's effect decreases compared to the laser fluctuation's. One more thing to notice is that the \dot{n}_- appears to be slightly higher than the $-\sqrt{n_-} \cos\theta_c$ term, both when cooling and heating, which is the consequence of the heating effect exerted by the $\langle r_-^2 \rangle$ -term in eq. (4.18).

4.2.3 Heating



(a) Phonons over time in both modes.

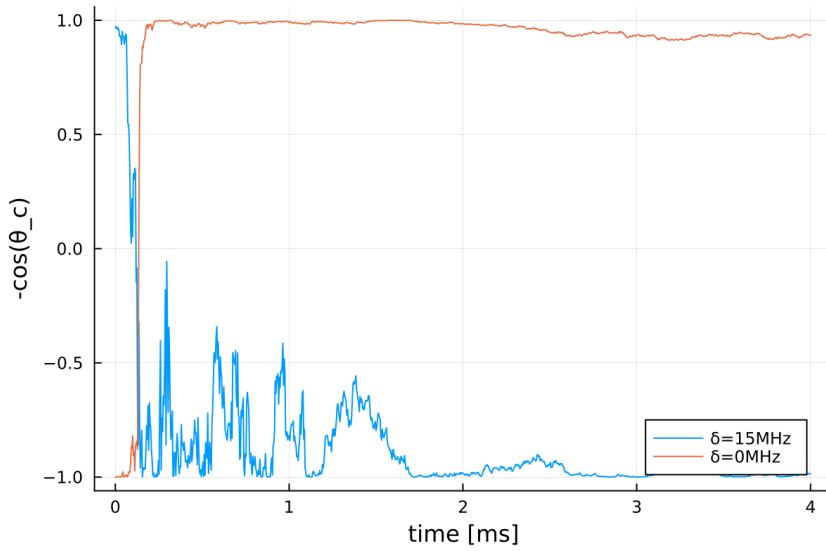
(b) The corresponding $-\cos(\vartheta_c)$.

Figure 4.3: Correlation check for θ_c and the number of phonons at $\omega_m = \omega_c$, $A_m = 2\pi \times 22$ MHz, $\delta_0 = 2\pi \times 15$ MHz and $\delta_0 = 2\pi \times 0$ MHz, $s_0 = 0.5$. The phase is 'locked' to π and 0, respectively, depending on whether the detuning is 'too big' or 'too small'.

Naturally, we ask ourselves what the phases behave like when we tweak the parameters such that (coupled) heating is observed. From eq. (4.18), we can predict that, neglecting the effect of $h(t)$, the cyclotron mode can experience heating only if $\theta_c \approx 0$ is fulfilled, meaning that it receives energy which is transferred from the magnetron mode.

Comparing this to the blue data points in fig. 4.3, where the detuning is set such that it is 'too big' (see also fig. 4.4, where we try different initial conditions on the phase), we see that this condition is clearly met, as θ_c locks to zero, initially fluctuating significantly. But the locking becomes highly stable once both modes have a high temperature. Theoretically speaking, excessive detuning will lead to a strong heating in the magnetron mode with a relatively weak coupling. Meanwhile, the cyclotron mode experiences strong cooling, but as the magnetron motion gets hotter, the heating of the cyclotron mode through the coupling will eventually outweigh this. The same effect can be observed when the axial frequency is increased, which agrees with the argument above: the coupling

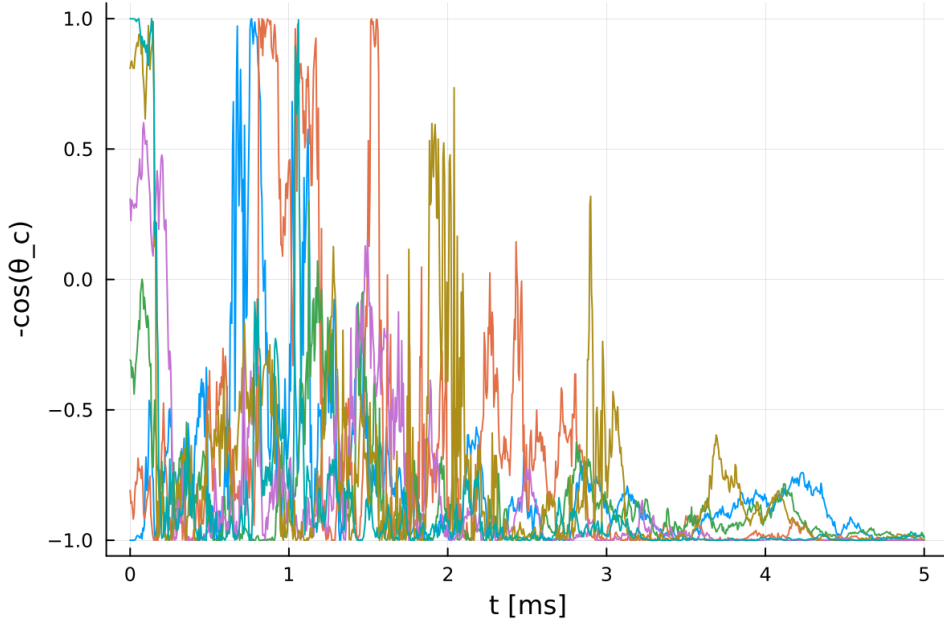


Figure 4.4: θ_c over time for varying initial phase at $\omega_m = \omega_c$, $A_m = 2\pi \times 22$ MHz, $\delta_0 = 2\pi \times 15$ MHz and $s_0 = 0.5$. The fluctuations die off once both modes are hot.

term for the magnetron mode's rate of change, which depends on ω_+ , becomes smaller relative to the self-sufficient term, which is proportional to ω_- . Therefore, the coupling can no longer compensate for the heating and will at some point lead to coupled heating in the cyclotron mode. This kind of heating can also occur if we do not set the detuning too high, but the phases are firmly locked.

However, when the detuning is 'too small', e.g. $\delta = 0$, which corresponds to the orange data points in fig. 4.3, the phase, θ_1 , will lock to zero in the case of $\omega_m = 2\omega_1$ and to π for $\omega_m = \omega_c$. Under these circumstances, we only get coupling which redirects energy from the cyclotron to the magnetron mode, where the magnetron mode's coupling rate is ω_+ and the cyclotron's is ω_- (see eq. 4.18). On top of that, the system experiences heating through the $h(t)$ term. However, the latter should not be enough to make the cyclotron grow and also is not necessary as we can observe the same behaviour when we look at a non-stochastic simulation with the radiation pressure force non-approximated (i.e. F_{RP} as in eq. 2.1). Thus, it seems that by making the Taylor-approximation, our description of the system loses the ability to explain this effect. Especially, the 'small velocity' approximation, made in eq. 4.6 will break down if one mode has a high temperature (which in this case is the magnetron) and, therefore, the consecutive treatment becomes inaccurate.

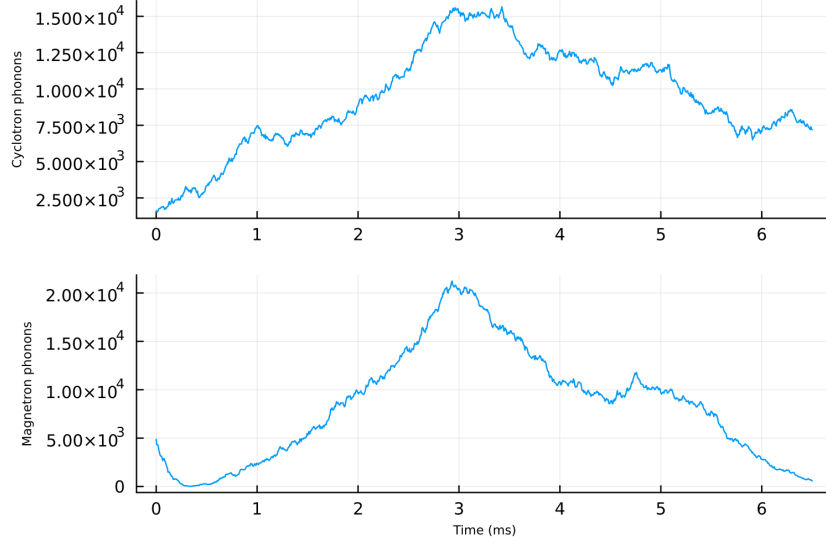
Looking back at figure 2.3, we now can associate the heating regions with the cases discussed in reference to fig. 4.3

4.3 Possibility for Different Cooling Schemes

Having gained a lot of insights into how the cooling works, we can think about different possibilities for cooling the ion.

4.3.1 Making Use of the Phase Control

Being able to synchronise the ions (even in case we are heating) possibly could be used in some scheme, as it gives us an unprecedented level of control over the ion. One option, which is explored in the following, is to alternate between pulses with no detuning and small detuning, while keeping a constant modulation amplitude. After each no-detuning pulse the ion's motional modes should be synchronised, i.e. its θ_1 should be around zero



(a) Phonons over time in both radial modes.

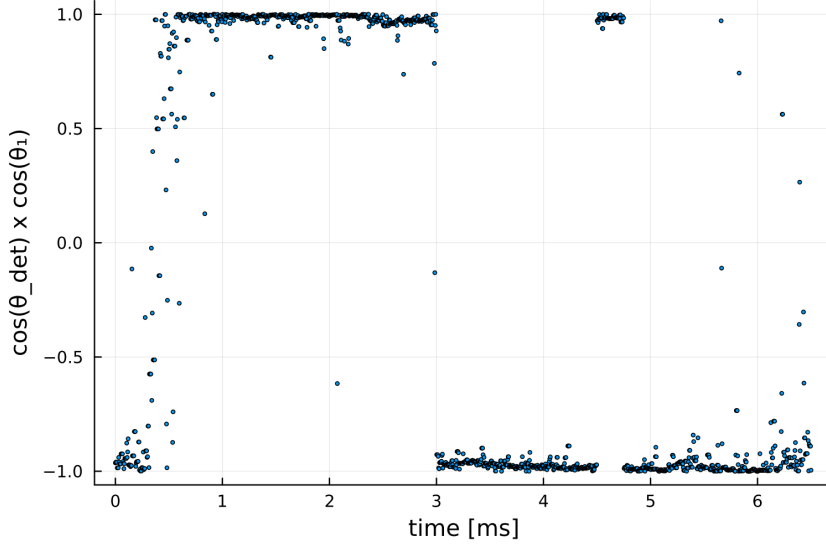

 (b) The corresponding ' θ_1 '.

Figure 4.5: Phase-controlling at $\omega_m = 2\omega_1$, $A_m = 2\pi \times 22$ MHz, $s_0 = 1.5$, alternating between $\delta_0 = 0$ MHz and $\delta_0 = 2\pi \times 4$ MHz. As long as neither of the modes goes too cold, we can control θ_1 .

(for $\omega_m = 2\omega_1$) with respect to the laser, as discussed in context of figure 4.3.

An illustration of what is meant by this verbal description is shown in figure 4.5. Here, the laser is designed to have zero detuning from 0 to 3 ms and from 4.5 to 4.75 ms, while during the rest of the time the detuning is 4 MHz. On top of that, we add a phaseshift of π to the modulation when changing the detuning, as no detuning locks θ_1 to zero, which leads to energy being coupled into the magnetron mode. Mathematically speaking, we add a time dependent phase $\theta_{det}(t)$ to the modulation term, i.e. $A_m \cos(\omega_{mod}t + \theta_{det}(t))$, where

$$\theta_{det}(t) = \begin{cases} \pi, \delta_0 \neq 0 \\ 0, \delta_0 = 0 \end{cases} . \quad (4.22)$$

While this does not affect θ_1 , it essentially flips the sign of the coupling term eq. (4.19), meaning that the magnetron motion is cooled only if $\cos \theta_{det}(t) \cos \theta_1 \approx -1$.

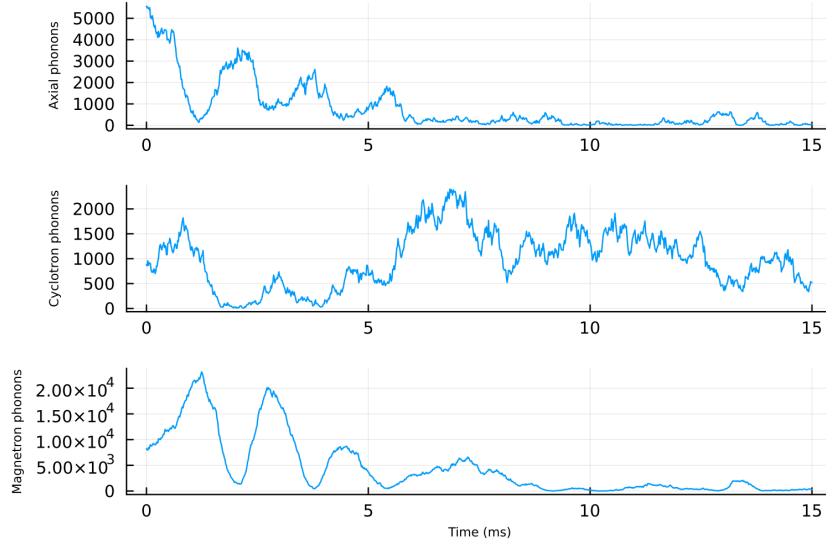


Figure 4.6: Phonons over time for varying initial phase at $\omega_m = \omega_- + \omega_z$, $A_m = 2\pi \times 62$ MHz, $\delta_0 = 2\pi \times 6$ MHz and $s_0 = 0.5$ with an additional axial unmodulated $\delta_z = 2\pi \times 6$ MHz, $s_0 = 0.013$ beam. Phonons are exchanged between the magnetron and the axial mode.

Studying θ_1 , we see that it starts around π and, consequently, is synchronised to 0, where it remains until the magnetron mode cools down to a lower temperature, after which the phase becomes increasingly random. But as long as the synchronisation is intact, we can easily control in which periods the ion is cooled or heated, i.e. the cooling and heating periods align closely with the defined detuning. We should keep in mind that the jumps in $\cos \theta_{det}(t) \cos \theta_1$ at 3 ms, 4.5 ms and 4.75 ms are due to the change in $\theta_{det}(t)$.

Although it is currently unclear how and if the magnetron mode could be brought to colder realms in a controlled manner, this is a first sketch of an idea of how the phase θ_1 could be possibly controlled, which then could improve the frequency modulation cooling.

4.3.2 Large Modulation Amplitude

When the modulation amplitude is very large, we observe phonon oscillations comparable to those in the non-stochastic, mean-force model, as depicted in fig. 3.2. We are now considering to try to use this for a cooling scheme. The underlying idea is to couple the magnetron to the axial mode through a highly-modulated beam and use a separate, axial, non-modulated beam to get rid of the phonons making use of standard Doppler cooling. This process seems to work relatively well for parameters of $A_m \approx 2\pi \times 60$ MHz, $\delta = \delta_z = 2\pi \times 6$ MHz, axial power at $s_0 = 0.013$ and modulated beam power at $s_0 = 0.5$ saturation intensity, as shown in figure 4.6. However, the cyclotron becomes and remains rather hot. One must note that the relation between the powers of the two beams and the detuning of the modulated beam needs to be set quite carefully. Indeed, we need to make sure that the axial is neither cooled too strongly nor too weakly, as the axial mode is needed for both cooling and for coupling the axial to the magnetron mode. Hence, if it gets too cold, the magnetron is no longer cooled.

Chapter 5

Stochastic Differential Equation and Cooling Limit

For the model of the linearised radiation pressure force, so far we have seen a cooling condition, we explored its mechanism and arrived at an expression for the cooling rate. To conclude the theoretical treatment, in this chapter, we want to find an expression for the limit we can achieve with this cooling scheme.

5.1 Approach

As in the preceding chapter, we aim to incorporate the randomness into the radiation pressure force and find the standard deviation of the amplitudes of the two modes to arrive at the cooling limit.

Once more, we do so by following the concepts presented in [11] and adapting them to our requirements. The idea is to start from eq. (3.1), but this time including the force fluctuations, as described in eq. (4.2). This leads to a Langevin-type equation. In a next step, we make use of the considerations from [11], where they derive that the force fluctuations can be treated as white noise (eq. A.12). We then move to Fourier space and find the transfer function between the input force fluctuation and the complex amplitudes of the two motional modes, assuming that the motion is in a steady state. Transforming back, we arrive at an expression for the standard deviation of the modes' amplitudes, $\langle |B_{\pm}|^2 \rangle$, which we can evaluate by using the fact that the correlation function of the force fluctuations is time-independent, i.e. $\langle F'_{RP}(t)F'_{RP}(t + \tau) \rangle$ is independent of t .

Ultimately, we want to use the obtained analytical result to find a quantitative result for the cooling limit, for which we want to use the bandstrengths c_0 and $c_{m,0}$ found in section 3.4.

5.2 Analytical Expression for the Cooling Limit

We start with eq. (3.1) and add the fluctuations to the mean-field radiation pressure force as in eq. (4.2) to arrive at

$$\ddot{u} + i\omega_c \dot{u} - \frac{\omega_z^2}{2} u = \Re[F_I(t, \mathbf{v})] \approx -c_0 (\dot{u} + \dot{\bar{u}}) - 2c_{m,0} \cos(\omega_m t) (\dot{u} + \dot{\bar{u}}) + F'_{RP}(t). \quad (5.1)$$

We essentially repeat the process from section 3.2.2, but leave the amplitudes B_{\pm} complex. Committing to $\omega_m = 2\omega_1$ (where the case of $\omega_m = \omega_c$ can be treated analogously), we find the system dynamics

$$\frac{d}{dt} \begin{bmatrix} B_+(t) \\ B_-(t) \end{bmatrix} = \frac{1}{2\omega_1} \begin{bmatrix} -c_0\omega_+ & -c_{m,0}\omega_- \\ c_{m,0}\omega_+ & c_0\omega_- \end{bmatrix} * \begin{bmatrix} B_+(t) \\ B_-(t) \end{bmatrix} + \frac{1}{2\omega_1 M} \begin{bmatrix} i f(t) e^{i2\omega_1 t} \\ i f(t) \end{bmatrix}, \quad (5.2)$$

where $f(t)$ denotes the force fluctuation in a frame rotating at the magnetron frequency: $f(t) = F'_{RP} e^{i\omega t}$. From this expression, we can recover the cooling conditions (3.13) when taking the eigenvalues of the matrix. For $\omega_m = \omega_c$, we replace the B -vector by $\begin{bmatrix} B_+ \\ B^\dagger \\ B_- \end{bmatrix}$.

5.2.1 To Frequency Space and Back

Taking the Laplace transform we find for the steady state (here we assume that the system is initially at rest)

$$B(s) = G(s)U(s), \quad (5.3)$$

where $U(s)$ is the transform of the force fluctuations and $G(s) = (sI - A)^{-1}$ is the transfer function. Analogously, assuming that the system is in a steady state to begin with, we can do the same trick with the Fourier transform. Then, the steady state, which is obtained in the cooling limit, is given by the inverse Fourier transform

$$B(t) = \frac{1}{2\pi} \int_{-\infty}^{\infty} d\omega G(i\omega) U(i\omega) e^{-i2\pi\omega t}, \quad (5.4)$$

where setting $s = i\omega$ can be considered as a re-scaling the time $t \rightarrow \frac{t}{2\pi}$. In order to now find $|B_\pm|^2$, we look for the diagonal entries of the matrix

$$\langle B(t)B^\dagger(t) \rangle = \frac{1}{4\pi^2} \int_{-\infty}^{\infty} d\omega \int_{-\infty}^{\infty} d\omega' G(i\omega) \langle U(i\omega)U(i\omega')^\dagger \rangle G(i\omega')^\dagger e^{i2\pi(\omega+\omega')t}, \quad (5.5)$$

where the ensemble average is constrained to the stochastic part of the expression. Following [11], we explore the Fourier-transforms of the force fluctuations further and define $\tilde{f}(t) := f e^{i2\omega_1 t}$ to find

$$\langle U(i\omega)U(i\omega')^\dagger \rangle = \left\langle \int_{-\infty}^{\infty} dt e^{-i2\pi(\omega-\omega')t} \int_{-\infty}^{\infty} d\tau e^{i2\pi\omega'\tau} \begin{bmatrix} \tilde{f}(t)\tilde{f}^\dagger(t+\tau) & \tilde{f}(t)f^\dagger(t+\tau) \\ f(t)\tilde{f}^\dagger(t+\tau) & f(t)f^\dagger(t+\tau) \end{bmatrix} \right\rangle. \quad (5.6)$$

The first integral amounts to a delta function because the correlation function in the second integral is independent of t . The value of the latter is derived in [11] in the appendix and it is equal to a constant power spectral density of

$$\frac{1}{4\omega_1^2 M^2} \int_{-\infty}^{\infty} d\tau e^{i2\pi\omega\tau} f(t)f^\dagger(t+\tau) = \frac{1}{4\omega_1^2 M} 4\gamma_s R(1 + f_{sr}) =: c_f, \quad (5.7)$$

where $[c_f] = m^2 s^{-1}$. Here, f_{sr} is the emission coefficient in radial direction, as described in (4.8), R is the kinetic energy absorbed by the ion from a scattering event

$$R := \frac{(\hbar k_0)^2}{2M} \quad (5.8)$$

and γ_s is the average (velocity- and also time-averaged over the modulation-period) scattering rate as in eq. (4.5):

$$\gamma_s = \left\langle \frac{I}{\hbar\omega(t)} \frac{\sigma_0 \Gamma^2}{4} \left(\frac{1}{\delta(t)^2 + \frac{\Gamma^2}{4}(1+s)} \right) \right\rangle_t, \quad (5.9)$$

where we include the effect of power broadening by including the saturation parameter s .

With respect to the off-diagonal terms in eq. (5.6) we have to keep in mind that we will additionally get factors of the form $e^{\pm i2\omega_1 t(t+\tau)}$, i.e. removing the tilde, the matrix can be rewritten as

$$\begin{bmatrix} f(t)f^\dagger(t+\tau) & f(t)f^\dagger(t+\tau)e^{i2\omega_1 t} \\ f(t)f^\dagger(t+\tau)e^{-i2\omega_1(t+\tau)} & f(t)f^\dagger(t+\tau) \end{bmatrix}, \quad (5.10)$$

where the rotation has the effect that the nonzero value in the δ -distribution is shifted. Overall, we then arrive at

$$\langle U(i\omega)U(i\omega')^\dagger \rangle = c_f 2\pi \begin{bmatrix} \delta(\omega - \omega') & \delta((\omega - \omega') - 2\omega_1) \\ \delta((\omega - \omega') + 2\omega_1) & \delta(\omega - \omega') \end{bmatrix}, \quad (5.11)$$

Calculating the integral in eq. (5.5), we arrive at the cooling limits $\langle |R_\pm|^2 \rangle$ on the diagonal. We do so by making use of the residue theorem and as before we stick to the low power limit where $c_0, c_{m,0} \ll \omega_1, \omega_-$ and neglect terms of the form $\frac{c_{(m),0}}{\omega_{1,-}}$ to find that

$$\langle |R_\pm|^2 \rangle = \frac{1}{2c_0\omega_\pm} \frac{c_{m,0}^2\omega_c \mp c_0^2 2\omega_1}{c_{m,0}^2 - c_0^2} c_f. \quad (5.12)$$

This expression naturally breaks down when ω_1 becomes so small or the power so large that the approximation $\frac{c_{(m),0}}{\omega_1} \approx 0$ loses its justification. Substituting for c_f , we can further evaluate the expression to

$$\langle |R_\pm|^2 \rangle = \frac{(1 + f_{sr})}{2c_0\omega_\pm\omega_1^2 M} \frac{c_{m,0}^2\omega_c \mp c_0^2 2\omega_1}{c_{m,0}^2 - c_0^2} \langle \gamma_s \rangle R. \quad (5.13)$$

At this point it does not make sense to substitute further as the expression becomes quite unreadable. However, if we retreat from the band-strength coefficients and try to move back to expressions in terms of detuning and modulation amplitude, further simplification is possible.

5.2.2 Approximating as in eq. (2.6)

To further simplify eq. (5.13), let us remind ourselves that in chapter 2 we associated the radiation pressure force bandstrength coefficients with

$$2c_0 \approx \frac{\hbar k^2 \Gamma^3 s}{4M} \frac{\delta_0}{\left(\delta_0^2 + \left(\frac{\Gamma}{2} \right)^2 (1+s) \right)^2}, \quad (5.14)$$

for the non-oscillating component and analogously

$$4c_{m,0} \approx \frac{\hbar k^2 \Gamma^3 s}{4M} \frac{A_m}{\left(\delta_0^2 + \left(\frac{\Gamma}{2} \right)^2 (1+s) \right)^2}, \quad (5.15)$$

for the component oscillating at the modulation frequency. Sticking to these expressions, eq. (5.12) can be further evaluated to

$$\langle |R_\pm|^2 \rangle \approx \frac{2\pi I_0}{2c\hbar^2 k^5 \Gamma} \left(\delta_0^2 + \frac{\Gamma^2}{4} (1+s) \right) \frac{A_m^2 \omega_c \mp 4\delta_0^2 2\omega_1}{\frac{\delta_0}{2} (A_m^2 - 4\delta_0^2)} \times \frac{1}{\omega_\pm \omega_1^2} R(1 + f_{sr}), \quad (5.16)$$

and substituting for the saturation intensity $I_0 = 2\pi^2 \hbar c \Gamma / 3\lambda^3$, we find

$$\langle |R_\pm|^2 \rangle \approx \left(\delta_0^2 + \frac{\Gamma^2}{4} (1+s) \right) \frac{A_m^2 \omega_c \mp 4\delta_0^2 2\omega_1}{\delta_0 (A_m^2 - 4\delta_0^2)} \times \frac{h}{12M\omega_\pm \omega_1^2} (1 + f_{sr}). \quad (5.17)$$

5.2.3 No Modulation

For no modulation, we can do the same treatment starting from eq. (5.2) with $c_{m,0} = 0$, to find the cooling limits:

$$\langle |R_{\pm}|^2 \rangle = \frac{2\omega_1}{c_0(\omega_c \pm 2\omega_1)} c_f. \quad (5.18)$$

However, this is unjustified in the magnetron mode's case, as there actually should not be any steady-state solution because the matrix has a positive eigenvalue (corresponding to the magnetron amplitude), and therefore $\lim_{t \rightarrow \infty} |B_-(t)| = \infty$. Then, the Fourier transform does not exist. For the cyclotron mode, this should be trustworthy and corresponds to eq. (5.12) for $c_{m,0} = 0$ and eq. (5.17) for $A_m = 0$. When the laser frequency is not modulated, the approximation in eq. (5.14) actually becomes an equality.

We can further insert c_f to check if the cyclotron cooling limit agrees with the one found in [11]. When comparing this to the steady state in eq. (56c), we find a discrepancy in the constant, where our calculated value is smaller by a factor of 2/3. This factor comes from us using $\sigma_0 = \frac{2\pi}{k^2}$, instead of $\sigma_0 = \frac{3\pi}{k^2}$. If we use the latter the factor in the denominator of eq. (5.17) becomes 8 (instead of 12) and we recover Wineland's expression.

5.3 Cooling Limit for Numerically Obtained Bandstrengths

We now want to assess the quality of the preceding calculations by comparing the cooling limit to the values obtained in the simulation, as is presented in figure 2.3 and for the linearised laser-ion interaction in figure 2.4.

Turning back to eq. (5.13), we find a numerical value for the theoretical cooling limits as a function of detuning and modulation amplitude by using the values for c_0 and $c_{m,0}$ obtained in section 3.4. The results are shown in figure 5.3. In the cases where the cooling condition ($0 < c_0 < c_{m,0}$) is not met, the limit is set to 100 and 1000, respectively. In this calculation, the trap frequency is set to 2 MHz and the saturation intensity to 0.1. As already discussed in section 3.4, when the modulation amplitude is too large, this effectively results in a blue detuning $c_0 < 0$, while a large detuning results in $c_0 > c_{m,0}$, thereby violating the other part of the cooling condition (3.13).

It is important to note that in this context, we are specifically considering the linearised radiation pressure force. Therefore, our focus now shifts towards comparing the limits to figure 2.4, which shows the results of the corresponding stochastic simulation. With respect to the cooling limit, in both theory and stochastic simulation we arrive at around 10 phonons in the cyclotron mode and around 250 phonons in the magnetron mode. Furthermore, the area in which frequency modulation cooling is observed also looks highly similar in both cases. In terms of cooling limit, the linearised laser-ion interaction agrees quite well with the non-linearised one, which is displayed in figure 2.3.

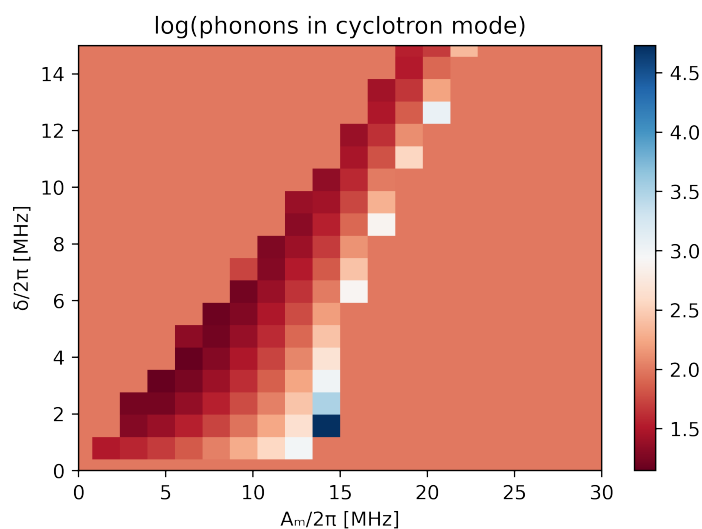
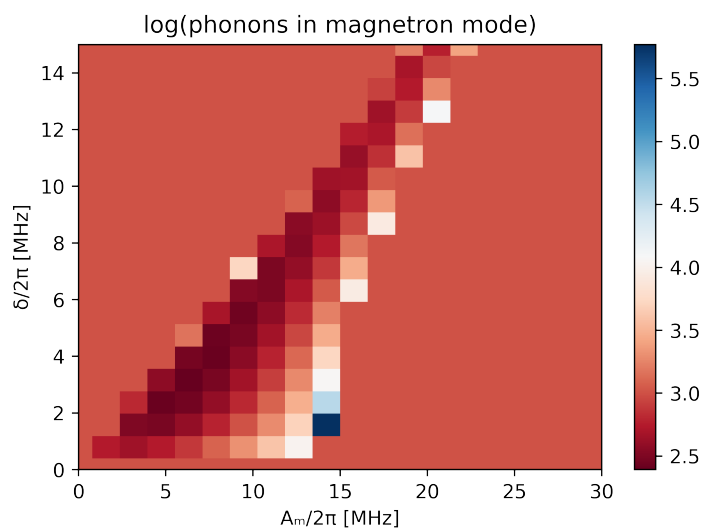
Figure 5.1: Cooling limit in the cyclotron mode as a function of δ_0 and A_m .Figure 5.2: Cooling limit in the magnetron mode as a function of δ_0 and A_m .

Figure 5.3: Numerical cooling limits as function of detuning and modulation amplitude, at $f_x = 2$ MHz trap frequency and $s = 0.1$ saturation intensity. In the region where the cooling condition (3.13) is not fulfilled, the limit was set to 100 and 1000, respectively. The limit lies around 10 phonons for the cyclotron and around 250 for the magnetron mode.

Chapter 6

Experimental Implementation and Results

The results obtained using the numerical simulations and the analytical theory were verified experimentally as follows in this chapter.

6.1 General Properties of the Setup

6.1.1 Penning Trap

The Penning trap used consists of a 3T superconducting solenoid magnet and the confining electric fields are generated by a micro-fabricated 2D-surface trap chip. For Doppler cooling, a single beam is used, which is at 45 degrees with respect to both radial plane and magnet axis, as shown in figure [6.1](#). As it has projections on both \hat{z} -axis and radial plane, this configuration suffices for affecting all the motional modes. The ions which are being trapped are Beryllium and the Doppler cooling beam, of 313 nm wavelength, is used for driving the $S_{1/2} \leftrightarrow P_{3/2}$ transition. Furthermore, a repumper is used, whose effect can be neglected because the ion leaves the cooling cycle at a very low rate.

A schematic of the TIQI Penning trap is shown in figure [6.2](#). To implement the modulation of the laser frequency, an EOM was added to the setup.

6.1.2 Cooling Scheme

The cooling scheme currently used in the TIQI Penning trap involves initially applying a ‘precooling’ pulse, during which the laser is red-detuned by approximately 600 MHz to the cooling transition and an axialisation potential is turned on. After that, the standard Doppler-cooling with axialisation is applied to bring the phonon numbers down to single-digits in all the motional modes, typically $\bar{n}_- \approx 8$ and $\bar{n}_+ \approx 5$. Starting from these temperatures, sideband cooling can be used to lower the temperature of the ion to the motional ground state. We now want to include the modulated cooling in this process, having it replace the axialised Doppler-cooling step. Theoretical analysis and simulation suggest that all three modes can be cooled simultaneously. However, for the magnetron mode, the cooling limit is expected to be high, i.e. around 250 phonons.

6.2 Converting Experimental Data to Phonon Numbers

To estimate the quality of a cooling scheme, the motional state of the ion is determined indirectly by reading out its ‘spin’-state. Starting in the $|up\rangle$ state, the probability of flipping the spin to $|down\rangle$ while driving the k th motional

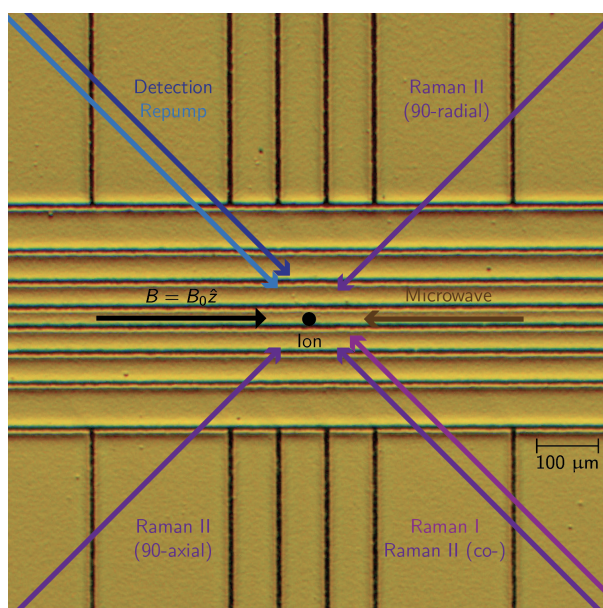


Figure 6.1: The beam configuration that was utilized and the trap surface. The cooling beam is denoted Detection, while the Raman beams control the qubit state. Figure by Shreyans Jain.

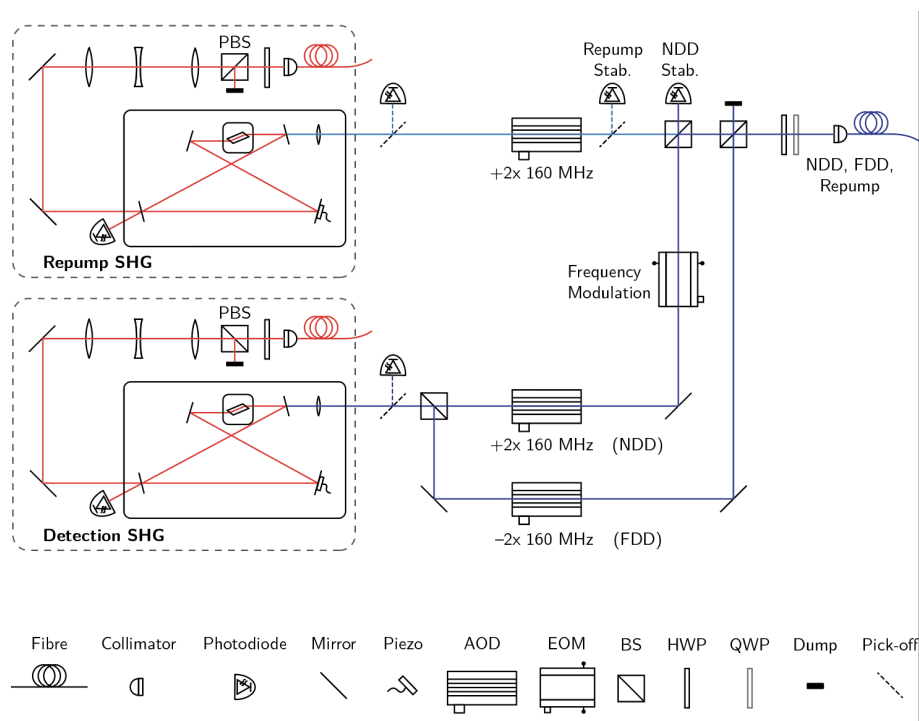


Figure 6.2: Experimental setup for generating the cooling and the repump beam. NDD denotes ‘near-detuned-detection’ and FDD represents the ‘far-detuned-detection’. The light entering the cavities has a wavelength of 626 nm, which is halved to 313 nm. Figure by Shreyans Jain.

sideband is measured. For the axial mode, the probability of not flipping the spin is theoretically given by

$$P(|up\rangle) = 1 - \sum_{n=0}^{\infty} \frac{\bar{n}^n}{(\bar{n}+1)^{n+1}} \frac{\Omega_{n,n+k}^2}{\Omega_{n,n+k}^2 + \Delta^2} \sin^2 \left(\frac{\sqrt{\Omega_{n,n+k}^2 + \Delta^2}}{2} t \right), \quad (6.1)$$

where Δ denotes the detuning from the transition and

$$\Omega_{n,n+k} = \left\langle n \left| e^{i\eta_z(\hat{a} + \hat{a}^\dagger)} \right| n+k \right\rangle = \Omega_0 e^{-\eta_z^2/2} (i\eta_z)^{|k|} L_m^{|k|}(\eta_z^2) \left[\frac{n!}{(n+k)!} \right]^{\text{sgn}(k)/2} \quad (6.2)$$

is the Rabi frequency of the k th motional sideband when the ion is initially in the Fock-state $|n\rangle$. η_z denotes the axial Lamb-Dicke parameter, Ω_0 is the carrier Rabi frequency, $L_m^{|k|}$ are the Laguerre polynomials [16], and $m = \text{Min}(n, n+k)$. The thermal distribution $\frac{\bar{n}^n}{(\bar{n}+1)^{n+1}}$ in eq. (6.1), on the other hand, describes the probability of being in $|n\rangle$, given that our mean phonon number is \bar{n} . As a consequence, given the experimental data Δ and t , we can make a fit with fitting parameter \bar{n} to find the phonon number of the ion and assess the quality of the cooling scheme (also, Ω_0 and the peak center are evaluated through the fit).

Meanwhile, the Rabi frequency associated with driving a sideband on either radial mode depends on the Fock-state number of both radial modes, since we simultaneously drive their transitions: $\Omega_{n,m,n',m'}$, where m and n denote the Fock state of the magnetron or cyclotron mode and m' and n' represent the respective sideband which is being driven. Starting in $|up\rangle$, the probability of not driving the transition is given by

$$P(|up\rangle) = 1 - \sum_{m=0}^{\infty} \sum_{n=0}^{\infty} \frac{\bar{n}^n}{(\bar{n}+1)^{n+1}} \frac{\bar{m}^m}{(\bar{m}+1)^{m+1}} \frac{\Omega_{n,m,n',m'}^2}{\Omega_{n,m,n',m'}^2 + \Delta^2} \sin^2 \left(\frac{\sqrt{\Omega_{n,m,n',m'}^2 + \Delta^2}}{2} t \right). \quad (6.3)$$

To evaluate the temperature of either radial mode, the excitation probability around its motional sidebands is measured, while the carrier of the other ‘spectator’ radial mode is driven, for example $n' = n$ and $m' = m + 1$ for the first blue sideband.

Graphically described, a cold state reveals itself by having vanishing higher-order sidebands (if the probe time t is set properly). This originates from the population distribution being shifted towards smaller $|n\rangle$ for low \bar{n} , where generally the higher-order sidebands come with lower Rabi-frequencies. In other words, the excitation probability decreases significantly with temperature for higher-order sidebands, while the effect on the carrier is smaller.

6.3 Results

Several scans were made in order to evaluate the capabilities of the frequency modulation cooling scheme. All measurements were carried out at a set axial frequency of 1.9 MHz, which for a magnetic field of 3 T yields a magnetron frequency of 381 kHz and cyclotron frequency of 4.737 MHz, summing to an unmodified cyclotron frequency of 5.118 MHz. The power of the laser was set through the AOM by tuning the input RF power, to where the frequency modulation cooling empirically seemed to work best.

6.3.1 Comparison to Precool

Based on the theory, we do not expect the modulated cooling to be as effective as the axialised Doppler-cooling, but we still aim to reach colder temperatures than during the pre-cooling stage. The comparison is made by turning off the Doppler cooling with the axialisation potential and observing the dips of the sidebands 0, +3, +6, +9 and +12 as a function of the duration of the modulated cooling pulse, as shown in fig. 6.3. The parameters used were -23 MHz red detuning and a modulation depth of 4.7, which corresponds to a modulation amplitude of roughly 24 MHz. We observe that the excitation probability increases gradually with an increasing pulse duration, which indicates

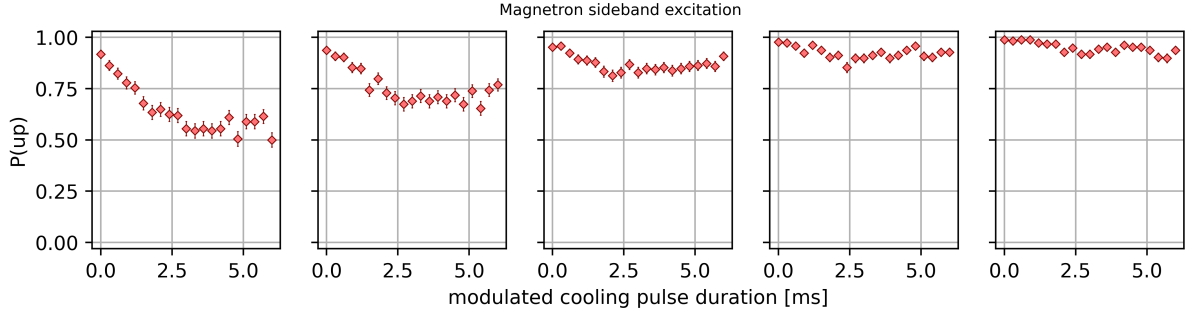


Figure 6.3: Excitation of the magnetron motional sidebands 0, +3, +6, +9, +12 (from left to right) as a function of the pulse duration of the modulated cooling following the precooling.

that the frequency modulation cooling brings an improvement over what the pre-cooling achieves. However, after around 3 ms of modulation cooling time, the excitation probability saturates for the investigated sidebands, and we can assume that the radial phonon numbers do not decrease any further for extended frequency modulation cooling pulse times.

6.3.2 Dependence on δ_0 and A_m

To check if we recover the theoretically predicted dependence on the detuning and the modulation amplitude, we can make a 2D-plot of the two variables, similar to fig. 2.3, which is shown in fig. 6.4. In this case, effective cooling is indicated by data points where the carrier excitation probability is relatively large, while the 12th sideband shows only a minor peak. In other words, we are looking for a large 12th sideband / carrier excitation probability ratio and we see such a region appear, similar to what is observed in the simulations. However, the region where cooling is the most efficient during the experiments appears to have shifted towards larger detunings.

6.3.3 Resonance

With this experimental setup, no signs of resonance have been observed. A scan over the modulation frequency, ω_m , is shown in figure 6.5, in which we see no significant difference in the excitation probabilities of the different bands. From the simulation, we would expect a different pattern to appear at a modulation frequency of $\omega_c = 5.118$ MHz, as presented in figure 2.1. Here, the red detuning was set to -25 MHz while a modulation depth of 4.7 was used. The parameters were selected based on experimental evidence indicating that frequency modulation cooling is the most efficient under these conditions.

Additional scans of the modulation frequency, similar to the one previously mentioned, were made for different detunings and EOM powers, scanning over different frequency regions, but those did not yield any result indicating a resonant dependence on the modulation frequency either.

6.3.4 Experimental Limits

Radial temperatures

In order to determine the experimental limit, the excitation probability is scanned as a function of detuning from the transition, Δ , for several sidebands and then \bar{n} is found by fitting eq. (6.3) to the spectra. This is done in figure 6.6 for a red $\delta_0 = -2\pi \times 21$ MHz and 4.7 modulation depth for the carrier and the magnetron blue motional sidebands +3, +6, +9, +12. From the fit parameters, we find that $\bar{n}_- = 280 \pm 30$ and $\bar{n}_+ = 3.1 \pm 0.3$. This agrees quantitatively with the simulation and the theory, despite the fact that the parameters at which modulation cooling works well do not coincide with the theoretical predictions.

As we cannot sum over an infinite amount of Fock-states, as proposed by the fitting function (6.3), we had to establish a cut-off point, which was chosen to be $|1000\rangle$. This implies that for a mean magnetron phonon number

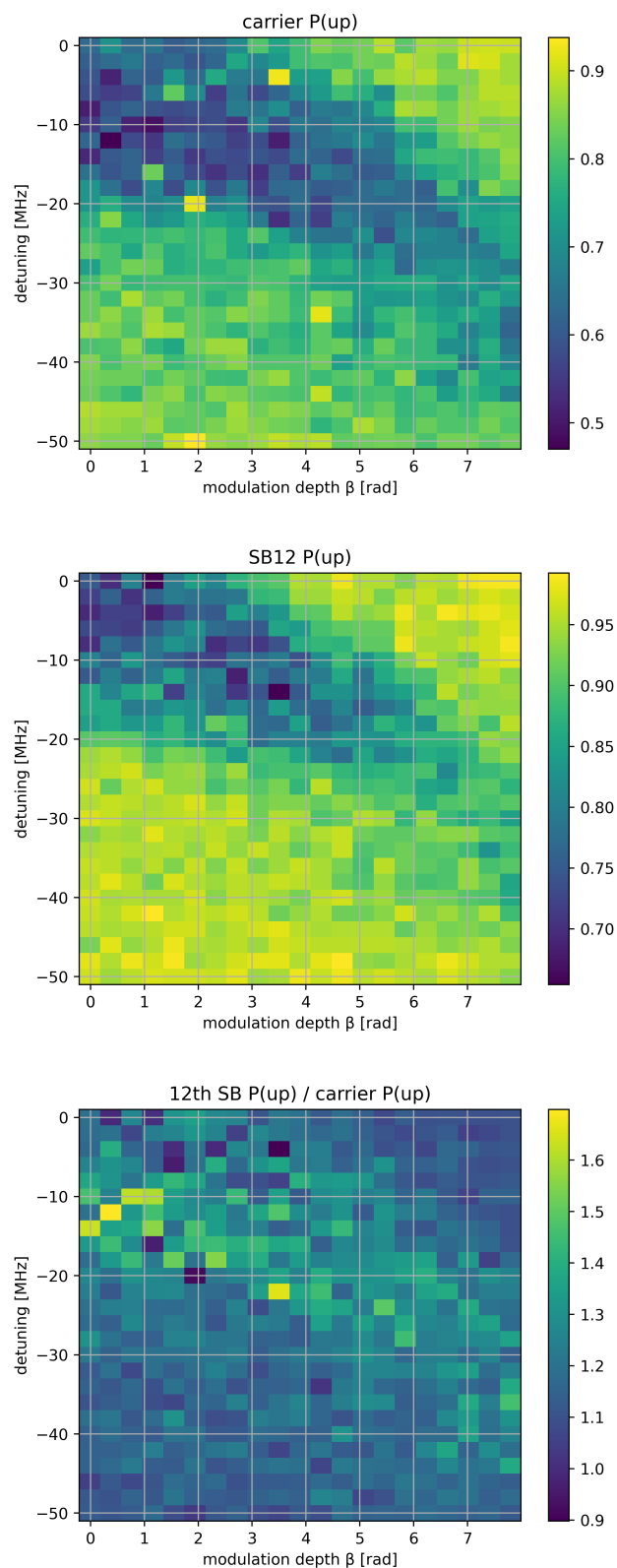


Figure 6.4: Experimental cooling as function of detuning and modulation amplitude. The ratio between the excitation probabilities of the sideband and the carrier is an indication of the coolest point, with a higher ratio corresponding to lower \bar{n}_- .

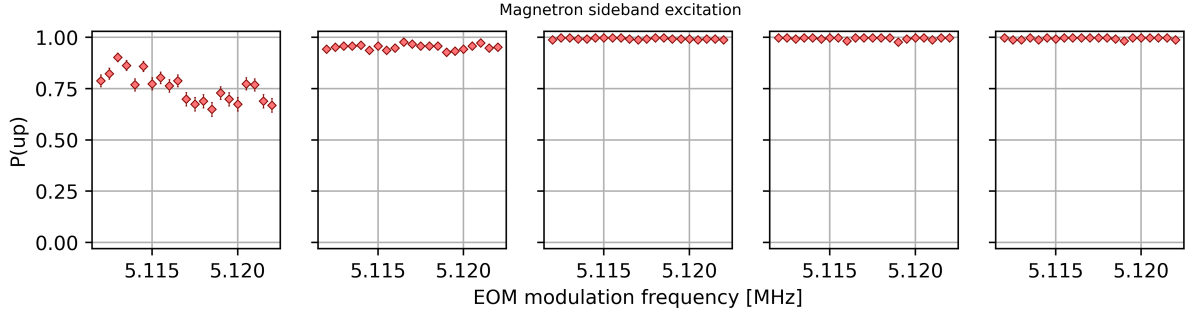


Figure 6.5: Excitation of the magnetron motional sidebands 0, +2, +4, +6, +8 (from left to right) as a function of the modulation frequency.

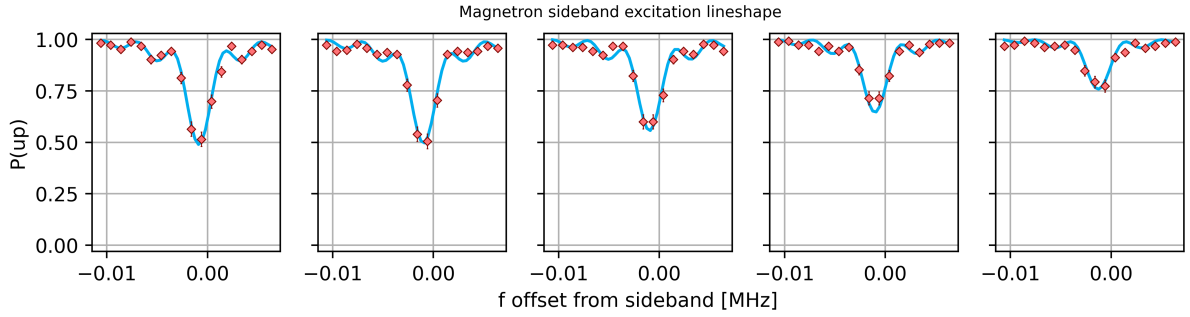


Figure 6.6: Excitation lineshapes of the magnetron motional sidebands 0, +3, +6, +9, +12 (from left to right). The number of included magnetron mode Fockstates is 1000. $\bar{n}_- = 280 \pm 30$ and $\bar{n}_+ = 3.1 \pm 0.3$.

of $\bar{n}_- = 280$, 97% of the Fock-population is included in the calculation, while the remaining lies in Fock-states $|n\rangle$ for $n > 1000$. For the cyclotron mode, the same number of Fock-states was included in the calculation, but as $\bar{n}_+ \ll \bar{n}_-$, the arising population loss is negligible.

Axial Temperature

Furthermore, we are interested in examining the minimum of the achievable temperature of the axial mode after using frequency modulation cooling. Again, we measure the excitation probability as a function of detuning for several sidebands. As the axial mode is much colder, we focus on the carrier and the red sidebands one to four. The temperature \bar{n}_z is evaluated by fitting eq. (6.1) to the obtained spectra. The result is shown in figure 6.7 and the extracted temperature is $\bar{n}_z = 6.8 \pm 0.4$. For this temperature, the sum over 150 Fock states accounts for more than 99% of the population. In this dataset, the red detuning was set to -24 MHz and the EOM was operated at

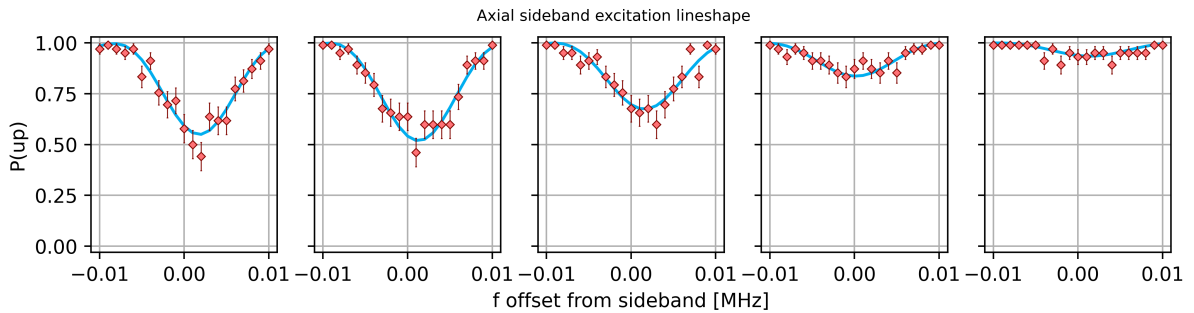


Figure 6.7: Excitation lineshapes of the axial red sidebands 0-4 (from left to right). The number of included axial Fockstates is 150. $\bar{n}_z = 6.8 \pm 0.4$.

a modulation depth of 4.7. Meanwhile, the theoretical Doppler cooling limit for the axial mode with this beam configuration is $\bar{n}_z = 4.2$, as can be derived from [11]. Hence, we can conclude that frequency modulation cooling achieves axial temperatures which are comparable to unmodulated, red-detuned Doppler cooling.

Chapter 7

Discussion

7.1 Theory

By neglecting the noise and linearising the ion-laser interaction, the phases of the frequency modulation cooled ion's magnetron and cyclotron motion synchronise to one of two values, between which they oscillate. The reason for this is that the laser frequency is modulated at either of $\omega_m = \omega_+ \pm \omega_-$, which couples the two motional modes. This results in a phonon exchange between the magnetron and the cyclotron mode, where the common synchronised phase $\theta_- \pm \theta_+$ determines which mode's energy is transferred into the other. Meanwhile, the red detuning ensures that overall energy is pulled out of the system through the cooling of the cyclotron mode. In that way, both radial modes can be cooled to a temperature close to the motional ground state, as long as $c_{m,0} > c_0$, which roughly corresponds to $A_m > 2\delta_0$.

Owing to the stochastic nature of photon scattering, the cooling process' effectiveness is diminished. A cooling limit of around 10 phonons in the cyclotron mode and 250 phonons in the magnetron mode is found, which aligns with what is observed in the simulation, both quantitatively and with regards to the parameters used. Unfortunately, this magnetron temperature is rather high for practical cooling applications. However, not relying on axialisation for cooling all the modes of motion may still prove to be useful in some experiments, which will be discussed in section [7.3.1](#).

Once higher orders in the Taylor approximation of the radiation pressure force are considered, the dynamics become more complicated. However, they naturally agree more with the simulation results obtained from the non-approximated expression.

7.2 Experiment

In the experimental implementation of the frequency modulation cooling scheme, we see that this brings a notable improvement in regards of ion temperature compared to the precooling stage of the TIQI Penning trap's cooling process. However, as already seen in the simulation, frequency modulation cooling cannot compete with axialisation Doppler cooling in terms of the achievable cooling limit for the magnetron mode. Setting the parameters to a red $\delta_0 = 2\pi \times 21$ MHz and $A_m = 4.7 \times \omega_c$, we can cool the ion down to 280 ± 30 phonons in the magnetron, 3.1 ± 0.3 in the cyclotron and 6.8 ± 0.4 in the axial mode. This result aligns with the theoretical cooling limits found for the linearised radiation pressure force and, also, with the values encountered in the stochastic simulations. In comparison to the precooling stage, all the three modes of motion get significantly colder when frequency modulation is appended. The cyclotron and the axial mode even achieve temperatures of the same order of magnitude as they do when Doppler cooling with axialisation is applied.

However, the theory was not entirely consistent with some observations. Most notably, no resonance effects were noticed in the experiment. Furthermore, the parameters for which the cooling appears to work best are

significantly different from the ones that were expected from the theoretical results. Specifically, the detuning is very large compared to the modulation amplitude. Meanwhile, the laser power seems to be highly relevant for the quality of the modulation cooling. No explanation has been found for these findings yet, assuming that the experiment works properly. However, the two former observations may be related in that the correct modulation frequency has not been tried yet in combination with an appropriate detuning and modulation amplitude. In this context, it would be interesting to simultaneously scan the detuning, the modulation amplitude, and the modulation frequency. That way, it could be ensured that the appropriate combinations of parameters are tried.

7.3 Outlook

One area that could still be theoretically explored further would be the higher order Taylor approximations of the laser-ion interaction, as discussed in section [3.5](#). So far, we have not examined this in the context of a fluctuating radiation pressure force. While it would increase the complexity of the calculations, it would also make the model of the physics more accurate.

On the experimental side, unanswered questions include why no resonance has been observed yet and why the experimental parameters at which the cooling works well do not match the theoretically predicted ones. Conducting simultaneous parameter scans as suggested may prove helpful to finding resonance effects.

7.3.1 Possible Applications

Although it seems that the modulation frequency cooling scheme is not potent enough for it to be practical in the process of getting an ion ground state-cold, i.e. for preparing the ion for resolved sideband cooling, it still may be useful for other applications. The advantage of this scheme is clearly the facility, with which one or several ions can be reached, as all it takes is one wide, red-detuned and frequency-modulated beam.

These findings may render the scheme interesting for applications where the ion's whereabouts change significantly during an experiment. In that case, the axialisation cooling does not work any more because the ion is far away from the field null. If the axialisation field is then turned on, this leads to a lot of excess micromotion, heating the ion significantly. Frequency modulation cooling, on the other hand, does not cool the ion to very low temperature limits but is also not expected to heat it.

A different possibility to make use of the scheme would be to use it for readout, as compared to driving the carrier, frequency modulation cooling does not heat up the ion much. Meanwhile, photons are still scattered similarly to when the carrier is driven. Hence, state readout could be performed without significantly heating the ion if a frequency-modulated and red-detuned beam was used.

Bibliography

- [1] R. Feynman, “Simulating physics with computers,” *International Journal of Theoretical Physics*, vol. 21, 1981.
- [2] P. Shor, “Algorithms for quantum computation: discrete logarithms and factoring,” in *Proceedings 35th Annual Symposium on Foundations of Computer Science*, pp. 124–134, 1994.
- [3] J. W. Britton, B. C. Sawyer, A. C. Keith, C.-C. J. Wang, J. K. Freericks, H. Uys, M. J. Biercuk, and J. J. Bollinger, “Engineered two-dimensional ising interactions in a trapped-ion quantum simulator with hundreds of spins,” *Nature*, vol. 484, pp. 489–492, Apr 2012.
- [4] J. I. Cirac and P. Zoller, “Quantum computations with cold trapped ions,” *Phys. Rev. Lett.*, vol. 74, pp. 4091–4094, May 1995.
- [5] C. Monroe, D. M. Meekhof, B. E. King, S. R. Jefferts, W. M. Itano, D. J. Wineland, and P. Gould, “Resolved-sideband raman cooling of a bound atom to the 3d zero-point energy,” *Phys. Rev. Lett.*, vol. 75, pp. 4011–4014, Nov 1995.
- [6] T. Hänsch and A. Schawlow, “Cooling of gases by laser radiation,” *Optics Communications*, vol. 13, no. 1, pp. 68–69, 1975.
- [7] G. Schneider, A. Mooser, M. Bohman, N. Schön, J. Harrington, T. Higuchi, H. Nagahama, S. Sellner, C. Smorra, K. Blaum, Y. Matsuda, W. Quint, J. Walz, and S. Ulmer, “Double-trap measurement of the proton magnetic moment at 0.3 parts per billion precision,” *Science*, vol. 358, pp. 1081–1084, Nov 2017.
- [8] S. Jain, J. Alonso, M. Grau, and J. Home, “Scalable arrays of micro-penning traps for quantum computing and simulation,” *Physical Review X*, vol. 10, Aug 2020.
- [9] G. Stutter, P. Hrmo, V. Jarlaud, M. Joshi, J. Goodwin, and R. Thompson, “Sideband cooling of small ion coulomb crystals in a penning trap,” *Journal of Modern Optics*, vol. 65, May 2017.
- [10] L. A. Zhukas, M. J. Millican, P. Svihra, A. Nomerotski, and B. B. Blinov, “Direct observation of ion micro-motion in a linear paul trap,” *Phys. Rev. A*, vol. 103, p. 023105, Feb 2021.
- [11] W. M. Itano and D. J. Wineland, “Laser cooling of ions stored in harmonic and penning traps,” *Phys. Rev. A*, vol. 25, pp. 35–54, Jan 1982.
- [12] P. K. Ghosh, *Ion traps*. International Series on Monographs in Physics, Clarendon Press, 1. ed. ed., 1995.
- [13] R. J. Hendricks, E. S. Phillips, D. M. Segal, and R. C. Thompson, “Laser cooling in the penning trap: an analytical model for cooling rates in the presence of an axializing field,” *Journal of Physics B: Atomic, Molecular and Optical Physics*, vol. 41, p. 035301, Jan 2008.
- [14] G. Stutter, P. Hrmo, V. Jarlaud, M. Joshi, J. Goodwin, and R. Thompson, “Sideband cooling of small ion coulomb crystals in a penning trap,” *Journal of Modern Optics*, vol. 65, 2017.

- [15] A. Pikovsky, M. Rosenblum, and J. Kurths, *Synchronization: A Universal Concept in Nonlinear Sciences*. Cambridge Nonlinear Science Series, Cambridge University Press, 2001.
- [16] K. E. Cahill and R. J. Glauber, "Ordered expansions in boson amplitude operators," *Phys. Rev.*, vol. 177, pp. 1857–1881, Jan 1969.